

## MATERIALS SCIENCE

## Direct visualization of anionic electrons in an electride reveals inhomogeneities

Qiang Zheng<sup>1,2†</sup>, Tianli Feng<sup>3,4†</sup>, Jordan A. Hachtel<sup>5†</sup>, Ryo Ishikawa<sup>6</sup>, Yongqiang Cheng<sup>7</sup>, Luke Daemen<sup>7</sup>, Jie Xing<sup>1</sup>, Juan Carlos Idrubo<sup>5</sup>, Jiaqiang Yan<sup>1</sup>, Naoya Shibata<sup>6</sup>, Yuichi Ikuhara<sup>6</sup>, Brian C. Sales<sup>1</sup>, Sokrates T. Pantelides<sup>3\*</sup>, Miaofang Chi<sup>5\*</sup>

Electrides are an unusual family of materials that feature loosely bonded electrons that occupy special interstitial sites and serve as anions. They are attracting increasing attention because of their wide range of exotic physical and chemical properties. Despite the critical role of the anionic electrons in inducing these properties, their presence has not been directly observed experimentally. Here, we visualize the columnar anionic electron density within the prototype electride  $Y_5Si_3$  with sub-angstrom spatial resolution using differential phase-contrast imaging in a scanning transmission electron microscope. The data further reveal an unexpected charge variation at different anionic sites. Density functional theory simulations show that the presence of trace H impurities is the cause of this inhomogeneity. The visualization and quantification of charge inhomogeneities in crystals will serve as valuable input in future theoretical predictions and experimental analysis of exotic properties in electrides and materials beyond.

## INTRODUCTION

Electrides are a unique class of compound materials that comprise a framework of cation and anion sublattices with a net positive effective charge that is compensated by “anionic electrons” that are loosely bonded and localized at interstitial sites, forming an effective anion sublattice (1–6). Starting in the 1980s, electrides were studied as bulk materials, with several seminal papers highlighting their potential for unconventional physical and chemical properties (1–6). In the past decade, electrides became the focus of a rapidly growing number of papers with the discovery of layered electrides (7, 8), in which the anionic electrons form sheets in the van der Waals gaps between atomic layers, exhibiting very high electron mobility, very small work function, and strong magnetic anisotropy. At about the same time, electrides with anionic electrons localized in one-dimensional (1D) channels gained prominence (9, 10). Very recently, several electrides have been predicted to feature topological behavior (11–13). Overall, anionic electrons in electrides have been demonstrated to exhibit catalytic activity (9, 14, 15), high mobility and unconventional magnetism (7, 8), superconductivity (16, 17), nontrivial topological behavior (11–13), and strong correlations (18) and to behave like solvated ions in solutions (19). Electrides have also been demonstrated to be good for storing hydrogen (20, 21). All these features nurture expectations for real applications. However, electrides have so far been characterized only with macroscopic experiments, such as measurements of the work function (1, 2, 5, 7), while the highly

localized anionic charge density has only been studied theoretically (4, 6, 11, 22–24).

Aberration-corrected scanning transmission electron microscopy (STEM) routinely achieves sub-angstrom resolution and has been applied to directly characterize the structural, chemical, and bonding properties of materials at the atomic scale (25–27). While conventional STEM techniques are insensitive to local variations in the charge density, phase-contrast imaging, such as inline electron holography, recently demonstrated the capability to visualize a 2D electron gas with a spatial resolution of several nanometers (28, 29). Concurrently, differential phase contrast (DPC) in STEM, which can be obtained by using either segmented detectors (30–32) or 4D-STEM data sets from a pixelated detector (33, 34), has recently been shown to map local electric fields and charge densities at an unprecedented sub-angstrom spatial resolution (30, 31, 33–36). That capability renders STEM-DPC a powerful potential technique for probing the atomic-scale localization of the charge density at anionic sites in electrides.

In this work, we use STEM-DPC to directly probe the charge density in the interstitial columns of  $Y_5Si_3$ , a prototype electride, using a pixelated detector (or 4D-STEM).  $Y_5Si_3$  contains spatially localized electrons within 1D channels of  $\sim 4$  Å diameter (9). Previous theoretical calculations determined that these electrons are loosely bonded, occupying electronic states near the Fermi energy, leading to catalytic reactivity for  $Y_5Si_3$  (9) and exotic quantum properties, such as superconductivity and Mott-insulating behavior in similar structures (17, 18, 37). Here, we use STEM-DPC to analyze the total charge density in  $Y_5Si_3$  and, more specifically, electrons that accumulate at the interstitial columns surrounded by hexagonal rings of six Y atoms. The STEM-DPC results are complemented by density functional theory (DFT) calculations of the electric field and charge density, yielding good agreement between the theoretical results and the experimental data averaged over a large number of columns. However, by analyzing a large field of view of the electride, we find an unexpected variance in the observed anionic charge density at different interstitial columns. DFT simulations suggest that the likely origin of the observed inhomogeneities are H impurities, which are

<sup>1</sup>Materials Science and Technology Division, Oak Ridge National Laboratory, Oak Ridge, TN 37831, USA. <sup>2</sup>Department of Materials Science and Engineering, The University of Tennessee, Knoxville, TN 37996, USA. <sup>3</sup>Department of Physics and Astronomy and Department of Electrical Engineering and Computer Science, Vanderbilt University, Nashville, TN 37235, USA. <sup>4</sup>Buildings and Transportation Science Division, Oak Ridge National Laboratory, Oak Ridge, TN 37831, USA. <sup>5</sup>Center for Nanophase Materials Sciences, Oak Ridge National Laboratory, Oak Ridge, TN 37831, USA. <sup>6</sup>Institute of Engineering Innovation, The University of Tokyo, 2-11-16 Yayoi, Tokyo 113-8656, Japan. <sup>7</sup>Neutron Scattering Division, Oak Ridge National Laboratory, Oak Ridge, TN 37831, USA.

\*Corresponding author. Email: chim@ornl.gov (M.C.); pantelides@vanderbilt.edu (S.T.P.)

†These authors contributed equally to this work.

known to be ubiquitous in materials, but often difficult to detect in small concentrations.

## RESULTS

### Crystal structure of $Y_5Si_3$

$Y_5Si_3$  crystallizes in a hexagonal  $Mn_5Si_3$ -type structure with the  $P6_3/mcm$  space group. Its structure in the  $[001]$  projection (Fig. 1A) shows six yttrium (Y) atomic columns forming hexagonal rings, each of which is composed of two alternating staggered layers of three Y triangles along the  $[001]$  projection. We have marked these atoms as  $Y_R$  on the schematic and the other Y sites as  $Y_1$  to help distinguish between the two for the remainder of the article. The centers of the Y rings form an interstitial column with a diameter of  $\sim 4$  Å.

$Y_5Si_3$  crystals were prepared by arc-melting high-purity Y and Si sources, following Lu *et al.* (9). A powder x-ray diffraction pattern (fig. S1) revealed the synthesized  $Y_5Si_3$  as being a single-phase system in the as-cast ingot, with refined lattice parameters [ $a = 8.4087(1)$  Å and  $c = 6.3422(1)$  Å] that are consistent with those in a previous report (9). The  $Y_5Si_3$  phase was air stable and water durable, as reported by Lu *et al.* (9). Ground fine powders were dispersed onto TEM grids in a helium-filled glovebox for the STEM experiments. TEM specimens are exposed to air during specimen loading, which is about 3 min.

### Electric field and charge density maps in $Y_5Si_3$

Figure 1B shows a high-angle annular dark-field (HAADF) image for a  $3 \text{ nm} \times 3 \text{ nm}$  region of  $Y_5Si_3$  oriented along the  $[001]$  axis. Owing to the  $Z$ -contrast nature of HAADF imaging (where  $Z$  is the atomic number), the intensity increases as the total number of atoms and/or their atomic number increase in each column. Thus, the brightest spots in the HAADF are the  $Y_1$  sites, which have double the number of Y atoms per unit cell as the  $Y_R$  sites. The  $Y_R$  atoms of the hexagonal ring are visible (and marked in the schematic in Fig. 1B), while the Si atoms are not observed in the HAADF images because of their proximity to the heavier Y atoms. The invisibility of Si atoms in HAADF images is confirmed by STEM image simulations, as shown in fig. S2.

In the DPC experiment, the electron beam is rastered across the region of interest (ROI) and the convergent-beam electron diffraction

(CBED) pattern is measured by a high-speed pixelated detector to form a 4D-STEM dataset. Because only the direct beam is used for 4D-STEM, a HAADF image can be acquired simultaneously without disrupting the DPC acquisition. For each probe position in the 4D-STEM dataset, the gradient of the electrostatic potential, i.e., the electric field in the sample, can be determined by measuring the shifts in the center of mass (CoM) of the CBED pattern. For thin objects, CoM shifts are proportional to the electric field experienced by the incident electron beam, allowing atomic-scale mapping of the local electric fields and charge densities (33, 35, 38).

Figure 2 shows a DPC acquisition of  $Y_5Si_3$  with an interstitial column in the middle. The simultaneously acquired HAADF image is shown in Fig. 2A. A schematic of how different signs of charge influence the CBED pattern and result in CoM shifts is shown in Fig. 2B; near a localized positive charge the incoming electron beam experiences a Coulomb attraction, whereas near a localized negative charge density the electron beam experiences Coulomb repulsion, while both result in a measurable shift of the distribution of electrons within the central disc of the CBED pattern.

The deflection of the beam in milliradians can be converted to a momentum transfer for each probe position, and for thin specimens (less than 5 nm), the momentum transfer can be quantitatively related to the projected electric field via Ehrenfest's theorem (38–40). Using position-averaged CBED (PACBED) from the dataset, we measured our sample to be  $\sim 7$  unit cells thick (corresponding to a thickness of 4.4 nm that is supported by electron-energy loss spectroscopy log-ratio analysis) (see figs. S3 and S4 for more details), allowing us to convert the CoM shifts into the projected electric field of the electrode, as shown in Fig. 2C.

At the  $Y_1$  sites, we observe the characteristic DPC profile of an atomic column corresponding to highly localized positive charge: a toroidal intensity profile, centered at the nucleus, with a radially outward directional profile. Although the CoM shifts corresponding to each probe position are the combined result from the electron cloud, the nuclei, and chemical bonding, it is the highly localized positive nuclear charges that dominate the atomic columns. However, the interstitial column is well isolated from its nearest atoms, i.e.,  $Y_R$  atoms. The distance between the interstitial column center to its nearest  $Y_R$  columns is  $\sim 2.05$  Å in the beam projection. The electric field surrounding the interstitial column center—i.e., the centers of the  $Y_R$  hexagonal ring—has the same toroidal intensity profile but

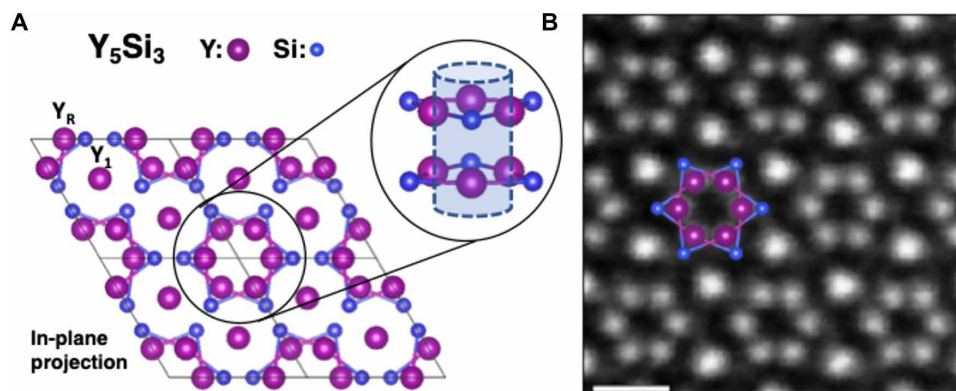


**Fig. 1. The crystal structure of electride  $Y_5Si_3$ .** (A) Schematic of the  $Y_5Si_3$  structure in the  $[001]$  projection. Black solid boxes indicate unit cells. Inset circles: Projected and side views of a hexagonal Y ring, with the center forming a column of electrons. (B) HAADF image of  $Y_5Si_3$  with overlaid atoms defining an interstitial electron column. Scale bar, 5 Å.

with a radially inward directional profile, indicating that the region contains spatially localized negative charge.

The projected electric field vectors can be converted to the projected charge density through Gauss's law, allowing us to examine the localization of charges directly and quantitatively, as plotted in Fig. 2D. As expected, the  $Y_1$  and  $Y_R$  sites are positive, corresponding to the high proton density, and are maximized at the positions of the nuclei, while in the interstitial column we observe a distinct negative charge density, consistent with the theoretically predicted anionic electrons for the electrone. We note that such an electric field profile could also be produced simply from probe tails interacting with the nuclei surrounding the site, as was reported previously for graphene (32). However, in this case, the contributions from the surrounding Y ring are mitigated because the implemented experimental probe size is  $\sim 1$  Å (full width at half maximum), while the distance between the six  $Y_R$  and the center of the interstitial site is much larger,  $\sim 2$  Å. To confirm the detection of anionic electrons, comparisons of DPC experimental results with the simulated charge density from DFT calculations can provide a trustworthy view of the charge density distribution in materials (34, 38, 39).

### Comparisons of DPC measurements with simulated charge density from DFT

To better understand the DPC measurements, DFT calculations were performed to determine the charge density in the interstitial columns

in  $Y_5Si_3$ . As shown in fig. S5, calculations confirm the presence of localized electrons in the interstitial columns. These interstitial electrons mainly sit within 1 eV from the Fermi energy (fig. S6) and are largely contributed by anionic electrons, as reported by Lu *et al.* (9).

Validation of DPC measurements is performed by comparing the experimental observations of an interstitial unit cell (Fig. 3A) with the total charge density map calculated using DFT calculations (Fig. 3B), which has been proven to be an effective method. Here, the DFT total charge density map (Fig. 3B) is constructed by combining the electron density (obtained directly from the DFT calculation) with the proton density (obtained from positions and charges of the point nuclei in the projected field of view). Both the electron and proton densities were convolved with a probe function to match the spatial resolution of the electron beam, before being combined to form the total charge density (see detailed methods in fig. S7). Pseudopotentials, which treat the nuclei and core electrons together as screened nuclei with finite radii, were used in calculations. All-electron DFT calculations were also performed to validate the use of pseudopotentials. As shown in fig. S8, the electric field profile and electron density at the interstitial region are both nearly identical to the results obtained from the pseudopotential calculations, confirming the reliability of the calculations.

As shown in Fig. 3, the charge density map from DPC measurements matches well with that from DFT calculations: Both exhibit

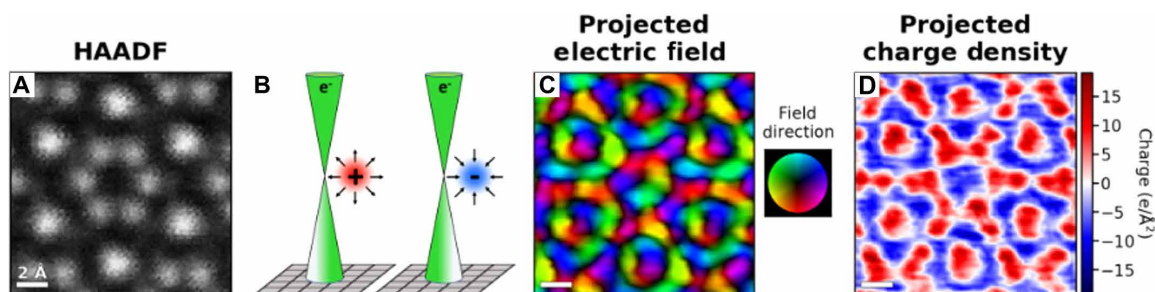


**Fig. 2. Differential phase contrast in  $Y_5Si_3$ .** (A) HAADF image of an interstitial column in  $Y_5Si_3$ . (B) Schematics for beam interaction with positive and negative charge densities generating CoM shifts. (C) Projected magnitude and direction of the electrostatic field in the sample as obtained from the CoM shifts. (D) Charge density derived from the divergence of the CoM shifts. The charge density color scale displays positive values on a white-to-red scale, negative values on a white-to-blue scale, and net zero charges as white. Note that the bonding electrons between Y and Si atoms are not discernible in (D) because of the broadened nuclear charges. The interstitial electrons, which are the focus of this work, are seen in blue in the column at the center of the map.

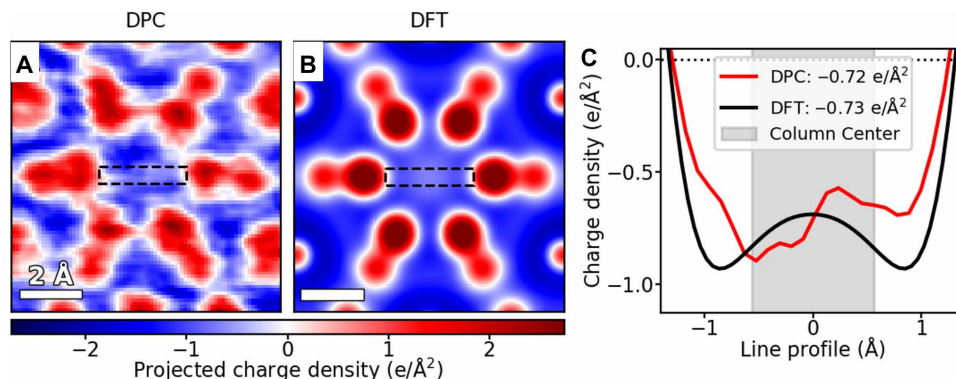


**Fig. 3. Quantitative comparison to theory.** The total charge density in an interstitial unit cell of  $Y_5Si_3$  as determined by (A) DPC and (B) DFT showing a strong qualitative match for the entire unit cell charge profile. (C) Line profiles [across the anionic column, from the regions highlighted with dashed lines in (A) and (B)] for both methods. The average charge density is calculated for the center (1-Å radius) region (marked by the gray area) of each interstitial column, demonstrating an excellent quantitative match between theory and experiment.

similar charge density profiles around a single unit cell; both consist of highly localized positive charge densities of the nuclei at each atomic site; both show a constantly negative charge density throughout the interstitial column; and both resolve the same spacing distances between the  $Y_1$  site and  $Y_R/Si$  atoms. These agreements are encouraging, as they indicate that the directions of the CoM shifts are consistent with the gradient of the potential. It has been shown that for samples that are too thick to perform quantitative DPC, the direction of the measured field tends to deviate notably (38).

Quantitative comparisons between DFT and DPC results are shown in Fig. 3C, where line profiles of the respective charge densities across the interstitial column are compared. While the DPC profile shows a slight asymmetry, the average experimental charge density at the column center is in excellent agreement with the calculated value,  $-0.73 \text{ e}/\text{\AA}^2$  for DFT and  $-0.72 \text{ e}/\text{\AA}^2$  for DPC, respectively. Methods of finding the center of the interstitial columns and averaging the column charge density are based on atomic positions obtained from corresponding simulated bright-field images and are described in detail in fig. S9. Results in Fig. 3 therefore demonstrate that DPC is sufficiently sensitive to probe local charge densities at the atomic scale, and comparisons of DPC and DFT measurements provide quantitative information of localized anionic electrons in electrides.

It is noted that, in contrast to the interstitial sites, relatively large intensity differences between DFT and DPC measurements are observed on Y sites. This disparity is largely induced by the dynamic scattering effect in electron imaging and the pseudopotentials adopted in the DFT calculations, because the former imposes a more dominant effect on heavy elements compared to light elements (38, 41, 42), while the latter treats the nuclei and core electrons together as screened nuclei with finite radii. While these factors likely do limit the quantitative comparison between the DPC and DFT results at the atomic sites, the region of the electride that we care most about, namely, the anionic electron columns, is spatially isolated from the atomic nuclei and is not influenced by dynamic scattering in this case.

### Inhomogeneity of anionic charge density in $Y_5Si_3$

The ability to quantitatively probe the electrons at the atomic scale allows us to examine the distribution of anionic electrons within the

specimen. The charge density map of a relatively large region, shown in Fig. 4A, reveals an unexpected phenomenon—the presence of a qualitative and quantitative inhomogeneity in the charge density profile across the different interstitial columns. Four distinct unit cells were highlighted in Fig. 4A for a further quantitative comparison. Horizontal line profiles of the average charge density in each unit cell are plotted against the corresponding profile from the DFT, as shown in Fig. 4 (B to E). The variation of charge density at the anionic electron sites (the intensity of the middle of the line profile) can be clearly seen. Unit cells C1 and C2 (Fig. 4, B and C) show a close quantitative match with the DFT column charge density, similar to that we analyzed in Fig. 3. Instead, unit cells C3 and C4 (Fig. 4, D and E) present a nearly neutral charge density at the center of the anionic column and deviate from the expected negative charge density. Quantitative analysis of spatial averaging of the charge densities within the center region of 1- $\text{\AA}$  radius allows us to further determine the average charge density of each cell to be 0.76, 0.75, 0.23, and 0.39  $\text{e}/\text{\AA}^2$ , respectively. Such an intensity variation suggests that most anionic columns have the predicted negative electron density, while some sites deviate from the pristine anionic charge density and show a lowered electron charge density. Further, these results also demonstrate that DPC not only is sensitive enough to probe small charge densities at the atomic scale but also enables direct atomistic analysis of the charge density in electrides through the combination with DFT calculations.

It is recognized that experimental artifacts could potentially be present in the measurements, but they are not likely to be the cause of the inhomogeneous charge density. First, the heterogeneity is randomly distributed across the 36 columns, while experimental artifacts, primarily induced by specimen thickness or beam illumination conditions, would vary in a rather continuous way. For instance, potential errors induced by beam tilts from scanning would induce systematic differences in the electric field between the top-left and bottom-right corners in each experimental map and introduce approximately the same effect to the interstitial columns as to their nearby atoms, neither of which was observed in our experimental data, as shown in Fig. 4A and figs. S10, S12, and S13.

In addition, no corresponding qualitative changes to the Y or Si intensities are associated with the DPC charge density variation in

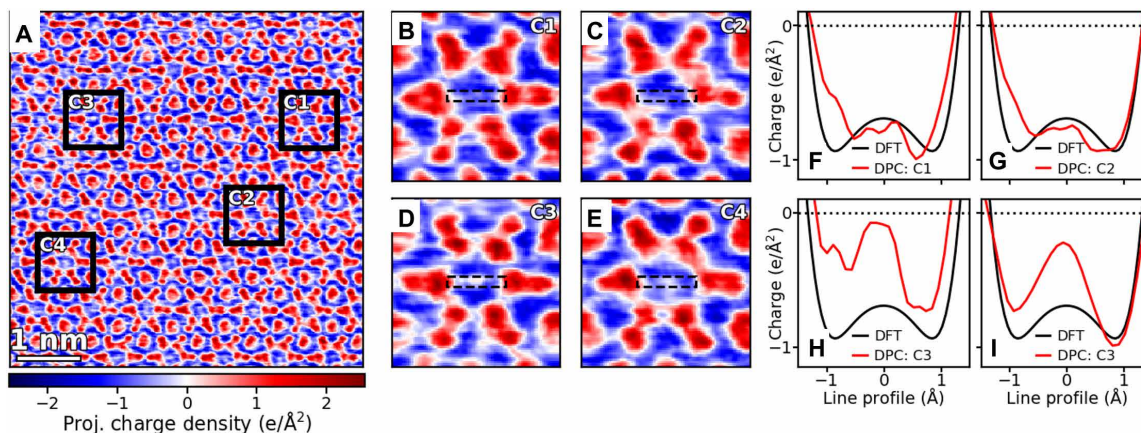


**Fig. 4. Inhomogeneity of anionic charge density of  $Y_5Si_3$ .** (A) Charge density map of a large area of  $Y_5Si_3$  showing an inconsistent profile across the center of the interstitial columns. (B to E) Zoomed-in views of columns having both the uniform negative electron density of the electride (B and C) and an inhomogeneity in the anionic electrons observed across the entire dataset (defined by a sharp peak of close to neutral charge density at interstitial column center) (D and E). (F to I) Line profiles across the column centers compared to the DFT line profile from Fig. 3, demonstrating that columns that do not show the inhomogeneity peak match quantitatively with the predicted DFT charge density (F and G), and the ones that have the inhomogeneity show the sharpest difference directly at the column center (H and I).

anionic columns, as shown in Fig. 4 (B to E) and fig. S10, where quantitative charge density of anionic columns and their surrounding  $Y_R$  from a larger region of the specimen are shown to confirm that there is no correlation between the column and its surrounding  $Y_R$  charge densities. Such an independence between the variations in interstitial columns and their neighboring  $Y_R$  columns again indicates that electron beam (e.g., scanning noise and beam tilts), specimen thickness, and surface contamination are unlikely to be the cause.

Moreover, the variation in charge density distributions is higher for Y columns compared to that of interstitial columns, which were calculated to be  $\pm 35\%$  for one of the  $Y_R$  columns and  $\pm 19\%$  for the interstitial columns, respectively (fig. S11), showing that the inhomogeneity observed among the interstitial columns is genuine. Further validation of the presence of charge variation among anionic columns is obtained by examining charge density maps from specimen regions with different thickness and using multiple different experimental conditions (fig. S12). The inhomogeneity is observed randomly distributed across the different columns in every dataset, demonstrating that the effect can be observed repeatedly and that it is real.

Furthermore, the inhomogeneity among the interstitial columns is also proved not to originate from scanning noise, as shown in fig. S13, which overlays the field shift directions on top of the charge density maps for a single unit cell that exhibits deviated charge density and for a unit cell that features the expected charge density. The field directions show that the charge density profile is consistent in both the fast-scanning ( $x$  direction) and slow-scanning ( $y$  direction) directions. These extensive tests and discussions indicate that while the presence of these potential effects cannot be completely excluded from our DPC experiments, neither of them could be the key cause of the observed inhomogeneity. Instead, such a large inhomogeneous distribution should be associated with a real feature in the material itself.

### Origin of charge density inhomogeneity in anionic columns

The column-resolved inhomogeneity could not have been observed in other experiments on electride materials, because, so far, only macroscopic techniques, which are insensitive to these local variations, have been used to characterize the presence of anionic charges.

Potential origins of the inhomogeneity in anionic columns are lattice defects in  $Y_R$  sites or impurity atoms at anionic sites. The contrast variation of  $Y_R$  atoms in STEM-HAADF images (e.g., Fig. 1B and figs. S2 and S3) is very small, while a missing  $Y_R$  atom should be clearly visible in STEM images if present, considering the specimen thickness, which only contains seven atoms in total per  $Y_R$  column. Impurity atoms are potentially present in the interstitial sites. Considering the zero contrast in STEM-HAADF and the small contrast in DPC images, the only possible impurity is hydrogen.

To illustrate the possibility that H atoms in the interstitial columns cause the observed inhomogeneity, we calculate the total charge density via DFT in the presence of different numbers of H atoms per interstitial column. Figure 5 (A to F) shows charge density plots in the cases of 0, 1, 2, 5, 10, and 20 H atoms per 10 unit cells, hence fractional values of 0, 0.1, 0.2, 0.5, 1, and 2 H atoms per interstitial site or half those values per formula unit (additional details shown in fig. S14). It can be seen that the charge density observed in the center of the column is sensitive to H concentrations. More critically, the incorporation of H results in a partial charge cancellation at the very center of the interstitial columns that is similar to the inhomogeneity observed in DPC. These total charge density maps are therefore directly comparable to the experimental maps obtained from DPC imaging. The intensity line profiles across their anionic columns are then plotted in Fig. 5G, and an apparent dependence of the charge density at the anionic site on the concentration of H can be seen. The charge density values averaged at the center of these reference interstitial columns (1-Å radius region) and their polynomial fits are further plotted in Fig. 5H, showing a nearly linear relationship between charge density and the concentration of H/site.

We can then use this relationship as a reference to estimate the H concentration of each single interstitial column in the specimen. The interstitial columns analyzed in Figs. 3 and 4 are plotted on this line to establish estimates for the H incorporation. The unit cells in Fig. 3, as well as those in Fig. 4 (B and C), are apparently pristine (zero H), while those in Fig. 4 (D and E), which showed a near neutral charge density at the column center, are estimated to have about 1.2 H and 1.9 H per interstitial site, respectively. Moreover, the average H integration of all interstitial columns in Fig. 4A can be

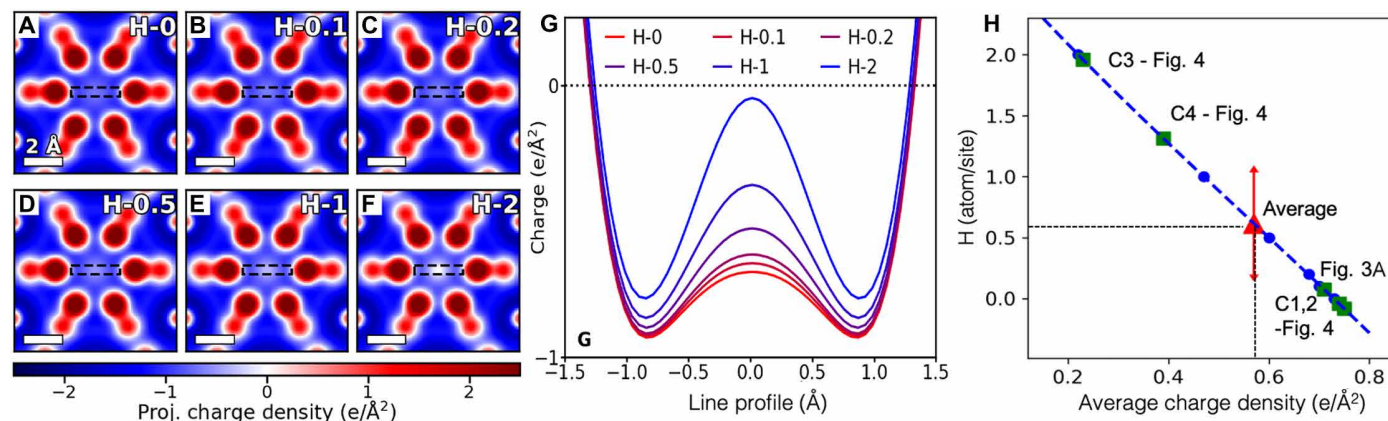


**Fig. 5. Quantitative charge density maps of  $Y_5Si_3$  with various H integrations.** (A to F) DFT calculated charge density maps (after probe convolution) with the integrations of 0, 0.1, 0.5, 1, and 2 H atoms per interstitial layer. (G) Line profiles across the column centers in (A) to (F), showing the dependence of charge density on the concentration of H at the anionic site. (H) Plot of average charge density within the central region (1-Å radius) of the interstitial column versus H concentrations based on (A) to (F). A nominal polynomial fit of the calculated charge density data (blue dots) is shown by a dashed blue curve. The experimental interstitial cells highlighted in Figs. 3 and 4 are plotted as green squares on this nominal line. The red triangle symbol represents the average H concentration in  $Y_5Si_3$  based on the experimental DPC of Fig. 4A, and its error bar is presented by the SD of all analyzed interstitial cells.

found on the plot as  $\sim 0.6$  H atom/site, on the basis of its average charge density of  $-0.56 e/\text{\AA}^2$  (fig. S11). In view of the ultrahigh synthesis temperature ( $>2000^\circ\text{C}$ ) and a very short time ambient exposure ( $\sim 3$  min) of the specimen, such a high fraction per site indicates that  $\text{Y}_5\text{Si}_3$  incorporates H atoms quite easily. This result is consistent with an earlier report that, under high  $\text{H}_2$  pressure and at an elevated temperature, the H concentrations in  $\text{Y}_5\text{Si}_3$  can be as high as six per formula unit (20). The energy barrier for a H atom to enter the interstitial column from the surface, calculated by manually stepping the H atom out of the crystal using DFT, is  $\sim 0.5$  eV (fig. S16), which is an upper bound so that more sophisticated calculations are not necessary. Such a barrier is sufficiently low for H to enter the lattice at room temperature, explaining experimental observations. The possibility of carbon contaminants, a common phenomenon during TEM observations, can be excluded because of the high positive contrast that even one single carbon atom can induce (fig. S15). Electronic excitations at room temperature can also be ruled out, because the density of excited electrons is relatively small even if one assumes that electronic excitations are local as opposed to Bloch-like. Therefore, H integration is most likely the cause for the inhomogeneity observed.

Inelastic neutron scattering (INS) spectroscopy (see Materials and Methods) was used to provide direct evidence for the presence of H in samples prepared using the same synthesis conditions and experiencing similar ambient exposure as the STEM sample. The result is shown in Fig. 6. To identify the peak position contributed by H, DFT phonon calculation was performed using Phonopy (43) for pristine  $\text{Y}_5\text{Si}_3$  and  $0.5\text{H}-\text{Y}_5\text{Si}_3$ . The results were used as input to the OCLIMAX software (44) to simulate INS spectra. The experimental spectrum is compared with the simulated spectra in Fig. 6. Here, we see that below  $\sim 350$   $\text{cm}^{-1}$  the vibrational response is dominated by Y and Si vibrational modes, and an excellent match is observed between the experiment and both the hydrogenated and pristine simulations. However, above  $350$   $\text{cm}^{-1}$ , no significant vibrational modes are observed in the pristine simulation, but in the hydrogenated simulation and the experiment, we see significant vibrational intensity in this regime, confirming the presence of a significant concentration of H in the material. The possibility of these two distinctive peaks originating from surface absorption of OH can be ruled out, as the typical frequency range for the vibration band of surface OH is  $400$  to  $1000$   $\text{cm}^{-1}$ , with strong intensities at

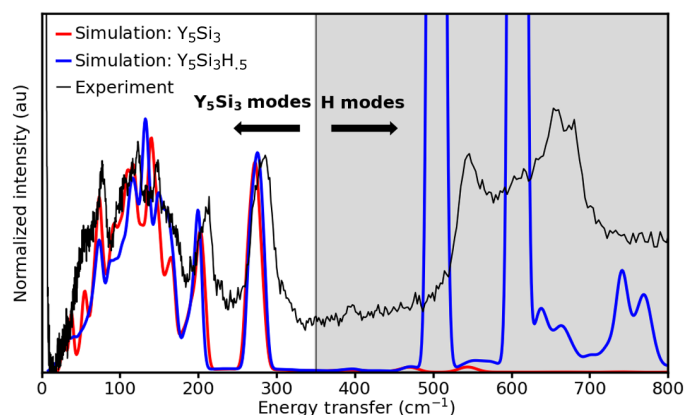


**Fig. 6. Inelastic neutron scattering spectroscopy.** Comparison of the measured INS spectrum with the simulated spectra for  $\text{Y}_5\text{Si}_3$  and  $\text{Y}_5\text{Si}_3\text{H}_{0.5}$ . au, arbitrary unit.

lower frequencies, and then decays with increasing frequency, a peak profile quite different from the experimental spectrum (45). The presence of two peaks observed in a similar frequency range in the experimental spectra proves the existence of H in the sample.

Using the simulations in Fig. 6, we estimated the H concentration in the sample, as measured by INS to be of order 0.2 H per site, which is within the error bars of the value of the DPC quantification shown in Fig. 5H,  $0.6 \pm 0.5$  H per site (there exists one site per two formula units). We note that the STEM experiments are performed on the absolute thinnest sample area (thickness,  $\sim 5$  nm), while the powder used for INS has predominantly micrometer-scale dimensions (fig. S17). Thus, the surface-to-volume ratio could play a significant role in the difference between the INS and DPC values. However, both techniques strongly indicate that a high concentration of hydrogen is present in the material and support the conclusion that H is the origin of the observed inhomogeneity in the measured anionic charge density.

## DISCUSSION

Our knowledge on anionic electrons in electrides, including their origin, distribution, and function, is still in its infancy. This work provides a technique that directly visualizes and quantifies anionic electrons, providing an unprecedented tool to the research of electrides. Detection and quantification of charge variation at anionic electron sites that is revealed and confirmed in this work can be used as input to the analysis of the exotic properties in electrides, in both experimental and theoretical studies, to help understand electrides better. The ability to directly probe spatially distributed electrons in materials opens up new opportunities to exploit real-space charge distributions, e.g., anionic electrons in electrides, the local charge redistribution caused by Moiré superlattices in bilayer 2D materials (46, 47), or the 2D electron gas that forms at some oxide interfaces (48, 49), to tailor these exciting materials for energy and quantum applications.

## MATERIALS AND METHODS

### Bulk sample preparation

Polycrystalline  $\text{Y}_5\text{Si}_3$  sample was prepared by directly arc-melting high-purity yttrium (99.99% pure; AMES) and Si (99.9999% pure; Alfa Aesar) elements with a molar ratio of 5:3 (9). Before melting, the arc-melter chamber was evacuated and back-filled with Ar for a few times. Zr was used as an oxygen getter and melted before Y and Si were arc-melted. The melted button was flipped over and remelted for five times to create a homogeneous sample. The weight loss during arc-melting was less than 0.1 mass %. The obtained ingot is extremely stable under air and also water durable (9). Nevertheless, after arc-melting, the ingot was transferred immediately into a He-filled glovebox for grinding and TEM specimen preparation.

### X-ray diffraction

Room temperature powder x-ray diffraction pattern was recorded on a PANalytical X'pert Pro MPD powder diffractometer using  $\text{Cu K}\alpha_1$  radiation. Powder data were analyzed using the WinCSD program package (50).

### STEM data acquisition

All the STEM data were acquired on a dedicated aberration-corrected Nion UltraSTEM100 equipped with a cold field-emission electron

source, operated at an accelerating voltage of 100 kV. The probe is  $\sim 20$  pA with a convergence semi-angle of 30 mrad. HAADF-STEM images were collected using the  $\sim 86$  to 200 mrad semi-angle range.

DPC imaging was performed on a Nion 2020 Ronchigram camera, with a Hamamatsu ORCA ultra-low noise scientific CMOS sensor and a  $2048 \times 2048$  pixel display. This camera can operate at a rate of 400 megapixels/second, with a readout noise of  $1.6$  well  $e^-$  (root mean square). The display readout capability for this camera is between dedicated pixelated detectors and direct electron detectors (33). The full detector is cropped to read out a  $48 \times 48$  pixel region for each Ronchigram. The acquisition time for all dataset in this work was 1 ms per Ronchigram image. The camera length of the microscope was adjusted to produce a diffraction plane calibration of 2.5 mrad per pixel.

DPC works by correlating the momentum transfer into the beam with the electric field experienced by the beam electrons. By using the pixelated detector, we can accurately measure the CoM of the CBED pattern, which, for extremely thin samples, corresponds to the momentum transfer because of the projected electric field in the material. Here, we use the thinnest observable regions in the electricle for our DPC analysis, and these areas are still thick for direct quantitative analysis for atomic columns of heavy elements but provide a strong qualitative match to theory for anionic electron columns (more details in later sections). By equating the direction and magnitude of the CoM shifts to the electric field, we can take the divergence of the electric field to find the crystal charge density through Gauss's law. The HAADF images were recorded simultaneously to the DPC datasets.

### DFT calculations

DFT calculations based on pseudopotentials were performed using the VASP package (51). All-electron DFT calculations were performed using ELK (52). We used the projector augmented wave (53) pseudopotential method and the Perdew-Burke-Ehrenhof (PBE) (54) generalized gradient approximation (GGA) for exchange and correlation. The GGA-PBE pseudopotentials are found to produce more accurate lattice constants than the local density approximation as shown in table S1. The unit cell was relaxed with a convergence of  $10^{-8}$  eV for the total energy and  $10^{-5}$  eV/Å for the forces on each atom. The plane-wave energy cutoff is 500 eV. The electronic  $k$ -space integration was performed with the tetrahedron method, involving a  $\Gamma$ -centered  $12 \times 12 \times 16$   $k$ -mesh. In the DFT calculations, the unit cell is divided into a  $128 \times 128 \times 6$  mesh for the charge density, electrostatic potential, and electric field. We also performed calculations using a  $2 \times 2 \times 1$  supercell. The resulting charge density, electric field, etc. are the same as using unit cell.

### HAADF and PACBED simulations

The HAADF image and PACBED simulations were performed using the frozen phonon model with a 100-kV probe with a probe-forming aperture semi-angle of 30 mrad via  $\mu$ STEM code (55). A supercell of  $67.2 \text{ \AA} \times 72.7 \text{ \AA}$  viewed along the [110] orientation comprising  $256 \times 256$  pixels was used. By comparing experimental PACBED with the simulations, we determined that the experimental specimen thickness is 7 unit cells ( $= 44.1 \text{ \AA}$ ) (fig. S3). The experimental defocus was set in the middle of the specimen thickness, and therefore, we used  $C_1 = 22 \text{ \AA}$  in the simulation.

### INS spectroscopy

The INS spectrum of the sample was measured at the VISION beam line at the Spallation Neutron Source (Oak Ridge National Laboratory),

an accelerator-based pulsed neutron source operating at 1.4-MW proton beam power. VISION is an inverted geometry spectrometer for neutron energy loss vibrational spectroscopy. It measures incident neutron energy by time of flight. The final neutron energy (3.5 meV) is set by a series of curved pyrolytic graphite mirrors. The dynamic range is from 0 to  $8000 \text{ cm}^{-1}$  with a nearly uniform resolution of 1 to 1.5% across this dynamic range. The sample was then cooled to 5 K in a top-loading, closed-cycle refrigerator at the beam line and measured for  $\sim 10$  hours. The spectrum of the empty sample holder was subtracted to obtain the signal from the sample. INS quantification is performed by using  $0.5\text{H-Y}_5\text{Si}_3$  as a reference and calculating the relative intensity of scattering by H versus that by the bulk crystal (energy transfer region, 20 to  $300 \text{ cm}^{-1}$ ).

### SUPPLEMENTARY MATERIALS

Supplementary material for this article is available at <http://advances.sciencemag.org/cgi/content/full/7/15/eabe6819/DC1>

### REFERENCES AND NOTES

1. S. B. Dawes, D. L. Ward, R. H. Huang, J. L. Dye, First electricle crystal structure. *J. Am. Chem. Soc.* **108**, 3534–3535 (1986).
2. R. H. Huang, M. K. Faber, K. J. Moeggenborg, D. L. Ward, J. L. Dye, Structure of  $\text{K}^+$  (cryptand[2.2.2]) electricle and evidence for trapped electron pairs. *Nature* **331**, 599–601 (1988).
3. J. L. Dye, Electricle: Ionic salts with electrons as the anions. *Science* **247**, 663–668 (1990).
4. D. J. Singh, H. Krakauer, C. Haas, W. E. Pickett, Theoretical determination that electrons act as anions in the electricle  $\text{Cs}^+$  (15-crown-5) $_2\text{e}^-$ . *Nature* **365**, 39–42 (1993).
5. M. J. Wagner, R. H. Huang, J. L. Eglin, J. L. Dye, An electricle with a large six-electron ring. *Nature* **368**, 726–729 (1994).
6. S. Matsuishi, Y. Toda, M. Miyakawa, K. Hayashi, T. Kamiya, M. Hirano, I. Tanaka, H. Hosono, High-density electron anions in a nanoporous single crystal:  $[\text{Ca}_{24}\text{Al}_{28}\text{O}_{64}]^{14+}\cdot 4\text{e}^-$ . *Science* **301**, 626–629 (2003).
7. K. Lee, S. W. Kim, Y. Toda, S. Matsuishi, H. Hosono, Dicalcium nitride as a two-dimensional electricle with an anionic electron layer. *Nature* **494**, 336–340 (2013).
8. J. Park, K. Lee, S. Y. Lee, C. N. Nandadasa, S. Kim, K. H. Lee, Y. H. Lee, H. Hosono, S.-G. Kim, S. W. Kim, Strong localization of anionic electrons at interlayer for electrical and magnetic anisotropy in two-dimensional  $\text{Y}_2\text{C}$  electricle. *J. Am. Chem. Soc.* **139**, 615–618 (2017).
9. Y. Lu, J. Li, T. Tada, Y. Toda, S. Ueda, T. Yokoyama, M. Kitano, H. Hosono, Water durable electricle  $\text{Y}_5\text{Si}_3$ : Electronic structure and catalytic activity for ammonia synthesis. *J. Am. Chem. Soc.* **138**, 3970–3973 (2016).
10. Y. Zhang, Z. Xiao, T. Kamiya, H. Hosono, Electron confinement in channel spaces for one-dimensional electricle. *J. Phys. Chem. Lett.* **6**, 4966–4971 (2015).
11. Y. Zhang, B. Wang, Y. Wang, L. Zhang, Y. Ma, Computer-assisted inverse design of inorganic electricles. *Phys. Rev. X* **7**, 011017 (2017).
12. C. Park, S. W. Kim, M. Yoon, First-principles prediction of new electricles with nontrivial band topology based on one-dimensional building blocks. *Phys. Rev. Lett.* **120**, 026401 (2018).
13. M. Hirayama, S. Matsuishi, H. Hosono, S. Murakami, Electricle as a new platform of topological materials. *Phys. Rev. X* **8**, 031067 (2018).
14. M. Kitano, Y. Inoue, Y. Yamazaki, F. Hayashi, S. Kanbara, S. Matsuishi, T. Yokoyama, S.-W. Kim, M. Hara, H. Hosono, Ammonia synthesis using a stable electricle as an electron donor and reversible hydrogen store. *Nat. Chem.* **4**, 934–940 (2012).
15. M. Kitano, S. Kanbara, Y. Inoue, N. Kuganathan, P. V. Sushko, T. Yokoyama, M. Hara, H. Hosono, Electricle support boosts nitrogen dissociation over ruthenium catalysis and shifts the bottleneck in ammonia synthesis. *Nat. Commun.* **6**, 6731 (2015).
16. M. Miyakawa, S. W. Kim, M. Hirano, Y. Kohama, H. Kawaji, T. Atake, H. Ikegami, K. Kono, H. Hosono, Superconductivity in an inorganic electricle  $12\text{CaO}\cdot 7\text{Al}_2\text{O}_3\cdot \text{e}^-$ . *J. Am. Chem. Soc.* **129**, 7270–7271 (2007).
17. Y. Zhang, B. Wang, Z. Xiao, Y. Lu, T. Kamiya, Y. Uwatoko, H. Kageyama, H. Hosono, Electricle and superconductivity behaviors in  $\text{Mn}_5\text{Si}_3$ -type intermetallics. *npj Quantum Mater.* **2**, 45 (2017).
18. Y. Lu, J. Wang, J. Li, J. Wu, S. Kanno, T. Tada, H. Hosono, Realization of Mott-insulating electricles in dimorphic  $\text{Yb}_5\text{Sb}_3$ . *Phys. Rev. B* **98**, 125128 (2018).
19. S. W. Kim, T. Shimoyama, H. Hosono, Solvated electrons in high-temperature melts and glasses of the room-temperature stable electricle  $[\text{Ca}_{24}\text{Al}_{28}\text{O}_{64}]^{14+}\cdot 4\text{e}^-$ . *Science* **333**, 71–74 (2011).
20. I. J. McCollm, V. Kotrocvo, T. W. Button, N. J. Clark, B. Bruer, Hydrogen sorption properties of  $\text{D}_{8g}$ -type systems: I. Hydrides of  $\text{Y}_5\text{Si}_3$ . *J. Less Common Met.* **115**, 113–125 (1986).

21. I. J. McColm, J. M. Ward, Hydrogen sorption properties of D8<sub>g</sub>-type systems: IV. Y<sub>5</sub>Ge<sub>3</sub> and Y<sub>5</sub>Si<sub>3</sub>-Y<sub>5</sub>Ge<sub>3</sub> solid solutions. *J. Alloys Compd.* **178**, 91–100 (1992).
22. X. Zhang, Z. Xiao, H. Lei, Y. Toda, S. Matsuishi, T. Kamiya, S. Ueda, H. Hosono, Two-dimensional transition-metal electride Y<sub>2</sub>C. *Chem. Mater.* **26**, 6638–6643 (2014).
23. T. Inoshita, S. Jeong, N. Hamada, H. Hosono, Exploration for two-dimensional electrides via database screening and Ab Initio Calculation. *Phys. Rev. X* **4**, 031023 (2014).
24. Y. Jing, Y. Ma, Y. Li, T. Heine, GeP<sub>3</sub>: A small indirect band Gap 2D crystal with high carrier mobility and strong interlayer quantum confinement. *Nano Lett.* **17**, 1833–1838 (2017).
25. T. Rojac, A. Bencan, G. Drazic, N. Sakamoto, H. Ursic, B. Jancar, G. Tavcar, M. Makarovic, J. Walker, B. Malic, D. Damjanovic, Domain-wall conduction in ferroelectric BiFeO<sub>3</sub> controlled by accumulation of charged defects. *Nat. Mater.* **16**, 322–327 (2017).
26. Y. Han, M.-Y. Li, G.-S. Jung, M. A. Marsalis, Z. Qin, M. J. Buehler, L.-J. Li, D. A. Muller, Sub-nanometre channels embedded in two-dimensional materials. *Nat. Mater.* **17**, 129–133 (2017).
27. O. L. Krivanek, M. F. Chisholm, V. Nicolosi, T. J. Pennycook, G. J. Corbin, N. Dellby, M. F. Murfitt, C. S. Own, Z. S. Szilagyi, M. P. Oxley, S. T. Pantelides, S. J. Pennycook, Atom-by-atom structural and chemical analysis by annular dark-field electron microscopy. *Nature* **464**, 571–574 (2010).
28. K. Song, S. Ryu, H. Lee, T. R. Paudel, C. T. Koch, B. Park, J. K. Lee, S.-Y. Choi, Y.-M. Kim, J. C. Kim, H. Y. Jeong, M. S. Rzechowski, E. Y. Tsymlar, C.-B. Eom, S. H. Oh, Direct imaging of the electron liquid at oxide interfaces. *Nat. Nanotechnol.* **13**, 198–203 (2018).
29. H. Lee, N. Campbell, J. Lee, T. J. Asel, T. R. Paudel, H. Zhou, J. W. Lee, B. Noesges, J. Seo, B. Park, L. J. Brillson, S. H. Oh, E. Y. Tsymlar, M. S. Rzechowski, C. B. Eom, Direct observation of a two-dimensional hole gas at oxide interfaces. *Nat. Mater.* **17**, 231–236 (2018).
30. N. Shibata, S. D. Findlay, Y. Kohno, H. Sawada, Y. Kondo, Y. Ikuhara, Differential phase-contrast microscopy at atomic resolution. *Nat. Phys.* **8**, 611–615 (2012).
31. N. Shibata, T. Seki, G. Sánchez-Santolino, S. D. Findlay, Y. Kohno, T. Matsumoto, R. Ishikawa, Y. Ikuhara, Electric field imaging of single atoms. *Nat. Commun.* **8**, 15631 (2017).
32. R. Ishikawa, S. D. Findlay, T. Seki, G. Sánchez-Santolino, Y. Kohno, Y. Ikuhara, N. Shibata, Direct electric field imaging of graphene defects. *Nat. Commun.* **9**, 3878 (2018).
33. J. A. Hachtel, J. C. Idrobo, M. Chi, Sub-Ångstrom electric field measurements on a universal detector in a scanning transmission electron microscope. *Adv. Struct. Chem. Imaging* **4**, 10 (2018).
34. S. Fang, Y. Wen, C. S. Allen, C. Ophus, G. G. D. Han, A. I. Kirkland, E. Kaxiras, J. H. Warner, Atomic electrostatic maps of 1D channels in 2D semiconductors using 4D scanning transmission electron microscopy. *Nat. Commun.* **10**, 1127 (2019).
35. K. Müller, F. F. Krause, A. Béché, M. Schowalter, V. Galioit, S. Löffler, J. Verbeeck, J. Zweck, P. Schattschneider, A. Rosenauer, Atomic electric fields revealed by a quantum mechanical approach to electron picodiffraction. *Nat. Commun.* **5**, 5653 (2014).
36. W. P. Gao, C. Addiego, H. Wang, X. Yan, Y. Hou, D. Ji, C. Heikes, Y. Zhang, L. Li, H. Huyen, T. Blum, T. Aoki, Y. Nie, D. G. Schlom, R. Wu, X. Pan, Real-space charge-density imaging with sub-ångström resolution by four-dimensional electron microscopy. *Nature* **575**, 480–484 (2019).
37. B. Lv, X. Y. Zhu, B. Lorenz, F. Y. Wei, Y. Y. Xue, Z. P. Yin, G. Kotliar, C. W. Chu, Superconductivity in the Mn<sub>5</sub>Si<sub>3</sub>-type Zr<sub>5</sub>Sb<sub>3</sub> system. *Phys. Rev. B* **88**, 134520 (2013).
38. K. Müller-Caspary, F. F. Krause, T. Grieb, S. Löffler, M. Schowalter, A. Béché, V. Galioit, D. Marquardt, J. Zweck, P. Schattschneider, J. Verbeeck, A. Rosenauer, Measurement of atomic electric fields and charge densities from average momentum transfers using scanning transmission electron microscopy. *Ultramicroscopy* **178**, 62–80 (2017).
39. G. Sánchez-Santolino, N. R. Lugg, T. Seki, R. Ishikawa, S. D. Findlay, Y. Kohno, Y. Kanitani, S. Tanaka, S. Tomiya, Y. Ikuhara, N. Shibata, Probing the internal atomic charge density distributions in real space. *ACS Nano* **12**, 8875–8881 (2018).
40. P. Ehrenfest, Bemerkung über die angenäherte Gültigkeit der klassischen Mechanik innerhalb der Quantenmechanik. *Z. Phys.* **45**, 455–457 (1927).
41. A. Lubk, J. Zweck, Differential phase contrast: An integral perspective. *Phys. Rev. A* **91**, 023805 (2015).
42. M. C. Cao, Y. M. Han, Z. Chen, Y. Jiang, K. X. Nguyen, E. Turgut, G. D. Fuchs, D. A. Muller, Theory and practice of electron diffraction from single atoms and extended objects using an EMPAD. *Microscopy* **67**, i150–i161 (2018).
43. A. Togo, I. Tanaka, First principles phonon calculations in materials science. *Scripta Mater.* **108**, 1–5 (2015).
44. Y. Q. Cheng, L. L. Daemen, A. I. Kolesnikov, A. J. Ramirez-Cuesta, Simulation of inelastic neutron scattering spectra using OCLIMAX. *J. Chem. Theory Comput.* **15**, 1974–1982 (2019).
45. Z. D. Hood, Y. Q. Cheng, S. F. Evans, S. P. Adhikari, M. P. Paranthaman, Unraveling the structural properties and dynamics of sulfonated solid acid carbon catalysts with neutron vibrational spectroscopy. *Catal. Today* **358**, 387–393 (2020).
46. E. C. Regan, D. Wang, C. Jin, M. I. B. Utama, B. Gao, X. Wei, S. Zhao, W. Zhao, Z. Zhang, K. Yumigeta, M. Blei, J. D. Carlström, K. Watanabe, T. Taniguchi, S. Tongay, M. Crommie, A. Zettl, F. Wang, Mott and generalized Wigner crystal states in WSe<sub>2</sub>/WS<sub>2</sub> moiré superlattices. *Nature* **579**, 359–363 (2020).
47. Y. H. Jiang, X. Y. Lai, K. Watanabe, T. Taniguchi, K. Haule, J. H. Mao, E. Y. Andrei, Charge order and broken rotational symmetry in magic-angle twisted bilayer graphene. *Nature* **573**, 91–95 (2019).
48. A. Ohtomo, H. Y. Hwang, A high-mobility electron gas at the LaAlO<sub>3</sub>/SrTiO<sub>3</sub> heterointerface. *Nature* **427**, 423–426 (2004).
49. S. Gariglio, N. Reyren, A. D. Caviglia, J.-M. Triscone, Superconductivity at the LaAlO<sub>3</sub>/SrTiO<sub>3</sub> interface. *J. Phys. Condens. Matter* **21**, 164213 (2009).
50. L. Akselrud, Y. Grin, WinCSD: Software package for crystallographic calculations (Version 4). *J. Appl. Cryst.* **47**, 803–805 (2014).
51. G. Kresse, J. Hafner, Ab initio molecular dynamics for liquid metals. *Phys. Rev. B* **47**, 558–561 (1993).
52. The Elk Code; <http://elk.sourceforge.net/>.
53. P. E. Blöchl, Projector augmented-wave method. *Phys. Rev. B* **50**, 17953–17979 (1994).
54. J. P. Perdew, K. Burke, M. Ernzerhof, Generalized gradient approximation made simple. *Phys. Rev. Lett.* **77**, 3865–3868 (1996).
55. L. J. Allen, A. J. D'Alfonso, S. D. Findlay, Modelling the inelastic scattering of fast electrons. *Ultramicroscopy* **151**, 11–22 (2015).
56. E. Parthé, The crystal structure of Y<sub>5</sub>Si<sub>3</sub> and Y<sub>5</sub>Ge<sub>3</sub>. *Acta Crystallogr.* **13**, 868–871 (1960).
57. H.-R. Zhang, R. F. Egerton, M. Malac, Local thickness measurement through scattering contrast and electron energy-loss spectroscopy. *Micron* **43**, 8–15 (2012).
58. J. Roger, M. Ben Yahia, V. Babizhetskyy, J. Bauer, S. Cordier, R. Guérin, K. Hiebl, X. Rocquefelte, J. Y. Saillard, J. F. Halet, Mn<sub>5</sub>Si<sub>3</sub>-type host-interstitial boron rare-earth metal silicide compounds RE<sub>5</sub>Si<sub>3</sub>: Crystal structures, physical properties and theoretical considerations. *J. Solid State Chem.* **179**, 2310–2328 (2006).
59. I. Mayer, I. Shidlovsky, M<sub>5</sub>X<sub>3</sub>-type rare earth silicides and germanides and their ternary phases with carbon. *Inorg. Chem.* **8**, 1240–1243 (1969).

**Acknowledgments:** M.C. gratefully acknowledges the valuable discussions and support from H. Hosono and his colleagues at the Tokyo Institute of Technology. **Funding:** The microscopy work was supported by an Early Career project supported by DOE Office of Science FWP #ERKZ55-KC040304. All microscopy technique development was performed and supported by Oak Ridge National Laboratory's (ORNL) Center for Nanophase Materials Sciences (CNMS), which is a DOE Office of Science User Facility. Q.Z., J.Y., and B.C.S. were supported by the U.S. Department of Energy (DOE), Office of Science, Basic Energy Sciences (BES), Materials Sciences and Engineering Division. Q.Z. thanks the partial support by the NSF-MRSEC. Theoretical work by T.F. and S.T.P. was supported, in part, by DOE grant DE-FG0209ER46554 and by the McMinn Endowment. Y.L., N.S., and R.I. were supported by the Nanotechnology Platform (project no. 12024046) from MEXT, Japan, JST-SENTAN, and JST-PRESTO, respectively. The computations partially used resources of the National Energy Research Scientific Computing Center, a DOE Office of Science User Facility funded through contract no. DE-AC02-05CH11231, and partially used the Extreme Science and Engineering Discovery Environment (XSEDE). The neutron scattering experiment was performed at ORNL's Spallation Neutron Source, supported by the Scientific User Facilities Division, Office of Basic Energy Sciences, U.S. DOE, under contract no. DE-AC0500OR22725 with UT Battelle, LLC. **Author contributions:** M.C. and Q.Z. conceived the project. Q.Z., J.Y., J.X., and B.C.S. synthesized the sample. Q.Z. and J.A.H. acquired the experimental data. T.F. and S.T.P. performed the DFT calculations. J.A.H. performed the experimental data analysis. R.I. performed image simulations. J.C.I. did initial image simulations. Q.Z., T.F., J.A.H., M.C., and S.T.P. prepared the manuscript. Y.C. and L.D. performed neutron scattering experiments. All authors were involved in the interpretation of data and the writing of the manuscript. **Competing interests:** The authors declare that they have no competing interests. **Data and materials availability:** All data needed to evaluate the conclusions in the paper are present in the paper and/or the Supplementary Materials. Additional data related to this paper may be requested from the authors.

Submitted 7 September 2020

Accepted 17 February 2021

Published 7 April 2021

10.1126/sciadv.abe6819

**Citation:** Q. Zheng, T. Feng, J. A. Hachtel, R. Ishikawa, Y. Cheng, L. Daemen, J. Xing, J. C. Idrobo, J. Yan, N. Shibata, Y. Ikuhara, B. C. Sales, S. T. Pantelides, M. Chi, Direct visualization of anionic electrons in an electride reveals inhomogeneities. *Sci. Adv.* **7**, eabe6819 (2021).

## Direct visualization of anionic electrons in an electrified surface reveals inhomogeneities

Qiang ZhengTianli FengJordan A. HachtelRyo IshikawaYongqiang ChengLuke DaemenJie XingJuan Carlos IdroboJiaqiang YanNaoya ShibataYuichi IkuharaBrian C. SalesSokrates T. PantelidesMiaofang Chi

*Sci. Adv.*, 7 (15), eabe6819. • DOI: 10.1126/sciadv.abe6819

### View the article online

<https://www.science.org/doi/10.1126/sciadv.abe6819>

### Permissions

<https://www.science.org/help/reprints-and-permissions>

Use of this article is subject to the [Terms of service](#)

---

*Science Advances* (ISSN 2375-2548) is published by the American Association for the Advancement of Science, 1200 New York Avenue NW, Washington, DC 20005. The title *Science Advances* is a registered trademark of AAAS.

Copyright © 2021 The Authors, some rights reserved; exclusive licensee American Association for the Advancement of Science. No claim to original U.S. Government Works. Distributed under a Creative Commons Attribution NonCommercial License 4.0 (CC BY-NC).

## Supplementary Materials for

### **Direct visualization of anionic electrons in an electride reveals inhomogeneities**

Qiang Zheng, Tianli Feng, Jordan A. Hachtel, Ryo Ishikawa, Yongqiang Cheng, Luke Daemen, Jie Xing, Juan Carlos Idrobo, Jiaqiang Yan, Naoya Shibata, Yuichi Ikuhara, Brian C. Sales, Sokrates T. Pantelides\*, Miaofang Chi\*

\*Corresponding author. Email: [chim@ornl.gov](mailto:chim@ornl.gov) (M.C.); [pantelides@vanderbilt.edu](mailto:pantelides@vanderbilt.edu) (S.T.P.)

Published 7 April 2021, *Sci. Adv.* **7**, eabe6819 (2021)  
DOI: 10.1126/sciadv.abe6819

#### **This PDF file includes:**

Figs. S1 to S17  
Table S1  
References

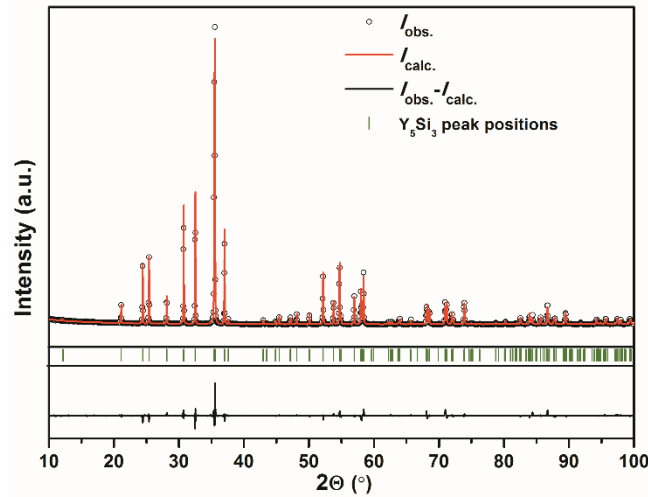


**Fig. S1. Powder X-ray diffraction (XRD) pattern for the as-cast  $Y_5Si_3$  sample.** The pattern was collected for ground powders, revealing the  $Y_5Si_3$  single phase in this sample. Experimental x-ray diffraction pattern (black dots) of the  $Y_5Si_3$  powder with the calculated profile (red lines) after full-profile Rietveld refinements. Peak positions of  $Y_5Si_3$  are given by green ticks; the difference plot is shown as a black line in the bottom. The full-profile Rietveld refinements were carried out using the structure model in Ref. (56) with the space group of  $P6_3/mcm$ . The refined lattice parameters are  $a = 8.4087(1) \text{ \AA}$  and  $c = 6.3422(1) \text{ \AA}$ . They are in good agreement with the previously reported values ( $a = 8.408(4) \text{ \AA}$  and  $c = 6.341(1) \text{ \AA}$  in Ref. (9)). This agreement indicates that besides Y and Si, the lattice for the arc-melted  $Y_5Si_3$  in this work contains few impurity elements.

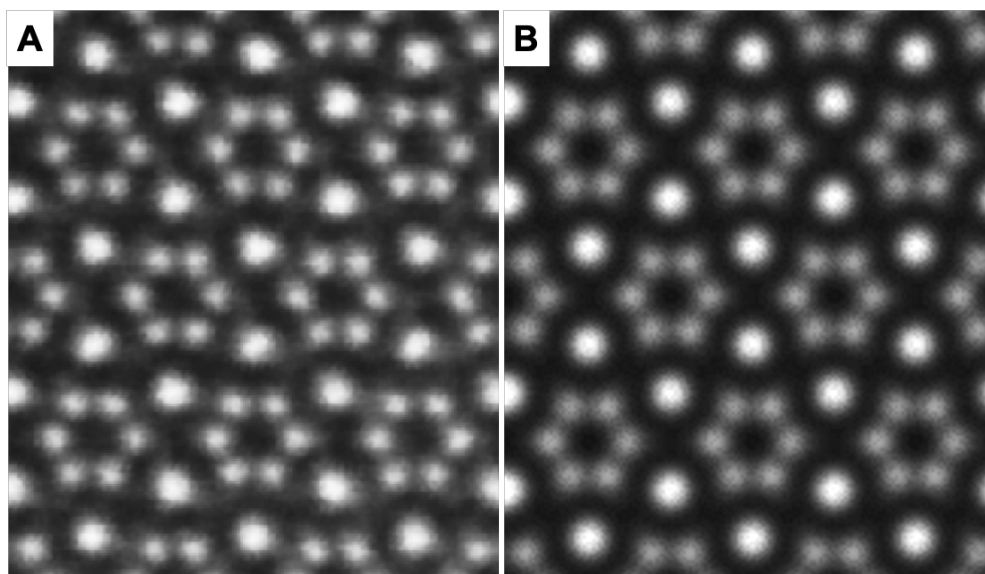


**Fig. S2. Comparison of STEM-HAADF images between experimental acquisition and simulation.** (A) Experimentally obtained image and (B) simulated image obtained by multi-slice image simulations, confirming the observed atomic structure of  $Y_5Si_3$ . The image simulation was performed with the  $\mu$ STEM code using experimental parameters regarding the probe, the defocus value, and the specimen thickness. Detailed information can be found in the Methods section. Scale bar: 1nm.

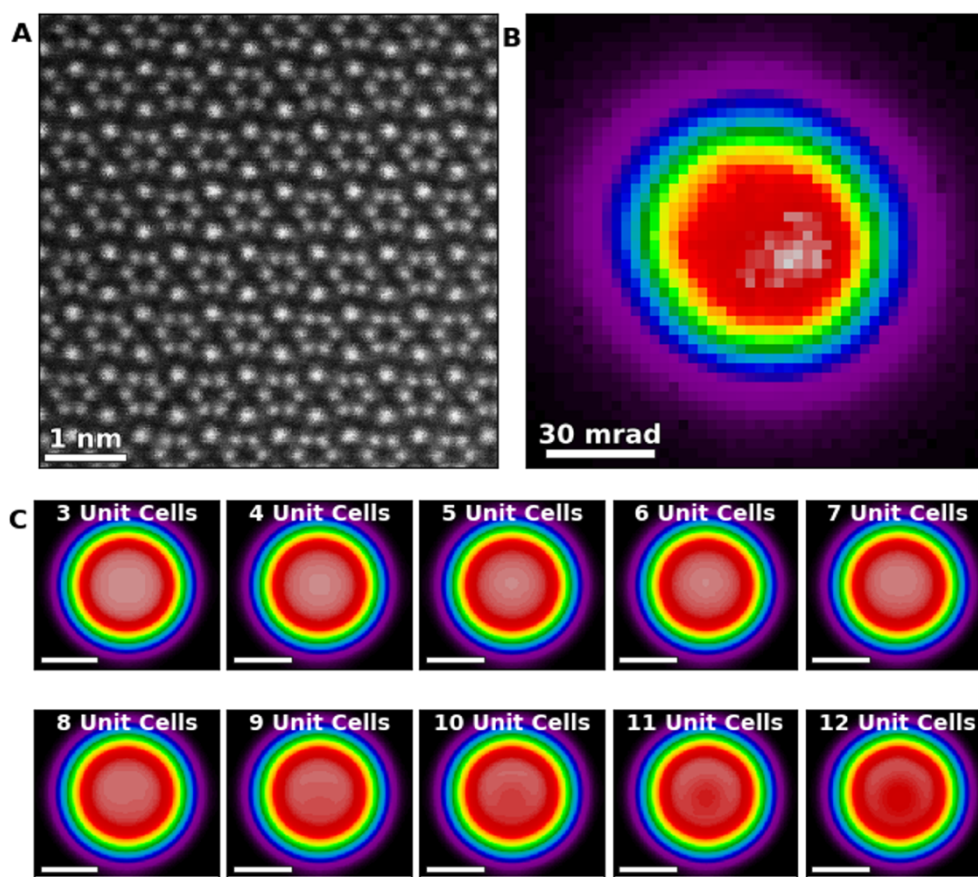


**Fig. S3. Estimation of specimen thickness *via* position-averaged CBED PACBED.** (A) HAADF image of the main region-of-interest ROI used in the main text for the 36 unit cell average. (B) PACBED for the 4D-STEM dataset acquired from this region. it is the average of the CBEDs acquired on the image with 512x512 pixels. (C) Simulated PACBEDs convolved with a 4 mrad gaussian blur to better compare to data for sample thicknesses of 3-12 unit cells. The thickness of the examined region of the specimen can then be determined by comparing the simulated PACBEDs with the experimental ones. These simulated PACBEDs are shown in (C) after the application of additional Gaussian blur by 4 mrad to account for the PSF of the small detector pixels. Here, the PACBED with low thicknesses has a uniform intensity throughout the central disk, with the intensity at the edges being highly comparable to the intensity at the center. As the thickness increases, the region of maximum intensity shrinks into the center of the bright field disk, but at 9 unit cells a dip becomes pronounced in the center of the bright field disk. By examining the experimental PACBED we see only the narrow high intensity region at the center of the BF disk with no pronounced dip, hence we believe that the sample cannot be thicker than 9 unit cells, and is mostly consistent with 7. It is clear by looking at the simulated PACBEDs that very little contrast that can be used to determine the thickness below 7 unit cells, so we believe that our data could be consistent with 6 and 8 unit cells, but not less than 6 or more than 8. So we select 7 as the most probable thickness for this region.

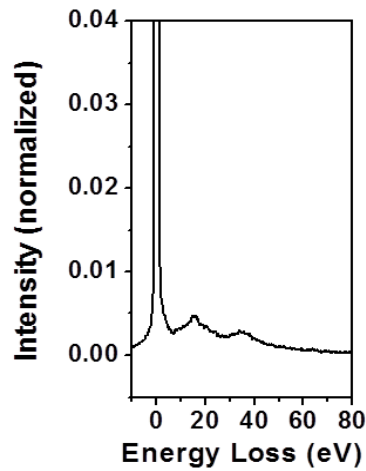


**Fig. S4. Thickness confirmation *via* Electron-energy loss (EEL) spectrum.** This EEL spectrum is an average spectrum of the specimen region where the 4D-STEM data were acquired. The low-loss spectrum was collected up to an energy loss of 360 eV, but only a part of the whole low-loss spectrum is shown. Spectra were collected using a Gatan Enfina spectrometer (Gatan Inc.), with collection semi-angle of 48 mrad and 0.3 eV/channel dispersion. The sample's thickness was calculated using the log-ratio method with an inelastic mean free path calculation. Here,  $\lambda$  was estimated to be  $\sim 50$  nm. EELS shows that the thickness in that region is  $0.11 t/\lambda$ . The corresponding total thickness for this region is thus  $\sim 5.4$  nm, which is slightly larger than the estimation from PACBED ( $\sim 4.4$  nm). This log-ratio method however has been shown to have errors of up to  $\sim 20\%$  in experiments with larger convergence angles and collection angles Ref (57), which corresponds to  $\sim 1$  nm for our experiments. These analyses, i.e. PACBED and EELS, leave us in a thickness regime in which qualitative DPC is feasible ( $\sim 5$  nm).

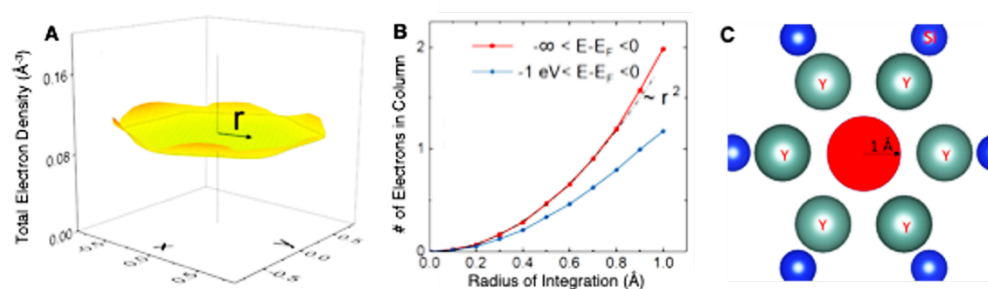


**Fig. S5. Electron density in the interstitial columns as a function of radius using DFT. (A)** 3D plot of uniform anionic electron density within interstitial columns. **(B)** Quantification of the number of electrons in the column as a function of radius from the center of the column, showing that the majority of the anionic electron density is within 1 eV of the Fermi level ( $E_F$ ). **(C)** Top view of the column to show the radius and its distance to the neighboring atoms. Note that the column center was used as the origin for the radius, and the DFT calculations were carried out without probe convolution.

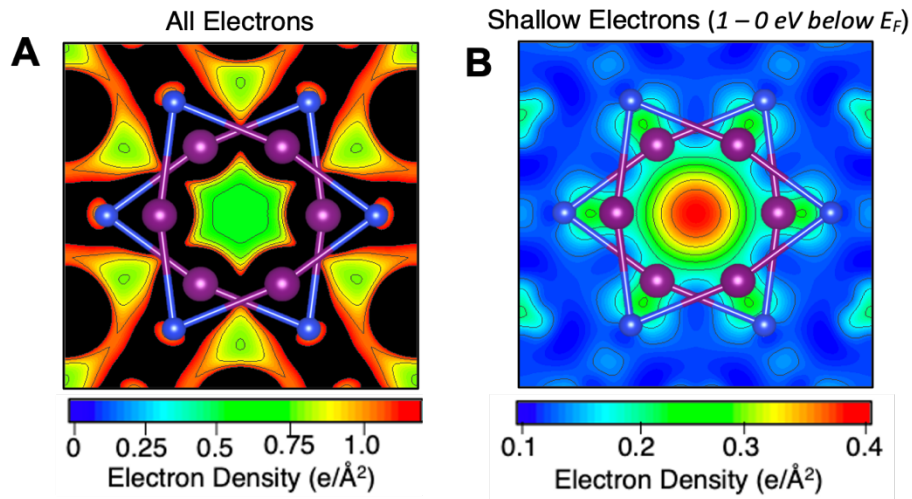


**Fig. S6. Electron accumulation at the interstitial site in  $Y_5Si_3$  revealed by DFT calculations.** (A) Two-dimensional electron density map (without probe convolution) along the [001] direction in  $Y_5Si_3$  with a thickness of one lattice unit cell, revealing the accumulation of electrons in the interstitial sites. (B) Electron density map (without probe convolution) of the shallow electronic states only (i.e. between 0 and 1 eV below the Fermi level) which reveals that most of the shallow electrons are concentrated in the interstitial region, and those electrons constitute the majority of the anionic electrons in  $Y_5Si_3$ , as reported by Lu. et. al. (9).

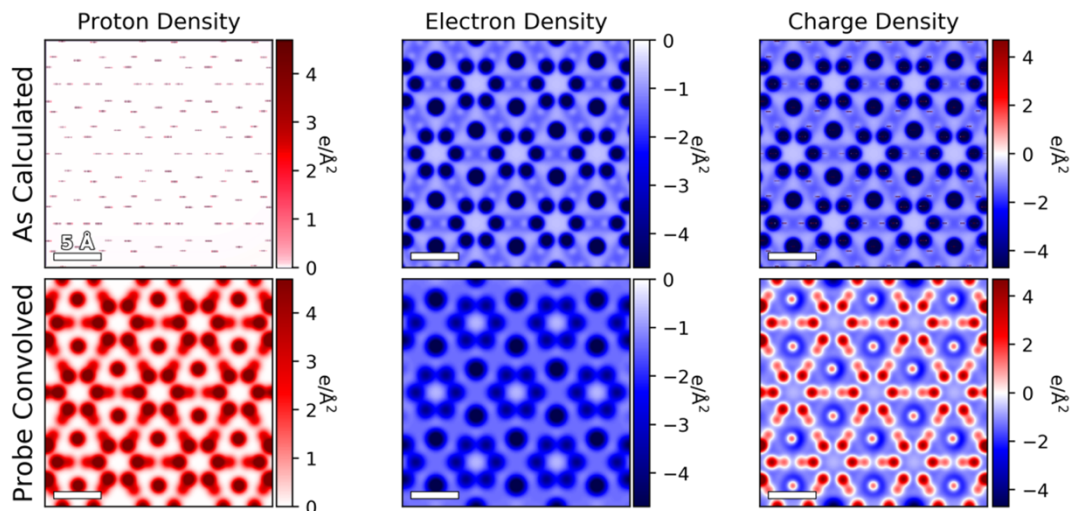


**Fig. S7. Calculations of DFT total charge density.** Proton density, electron density and charge density maps with and without probe convolutions. The total-charge-density map (bottom-right) was determined by combining the electron density (obtained directly from the DFT calculation) with the proton density (obtained from positions and charges of the point nuclei in the projected field-of-view). Both the electron and proton densities were convolved with a probe function to match the spatial resolution of the electron beam, before being combined to form the total charge density. Note that in order to show the overall charge distribution, the as-calculated charge density map here is *not* presented in the range between the minimum and the maximum, which are around  $300e/\text{\AA}^2$  at the Y sites, a value much larger than the charge density from electrons.

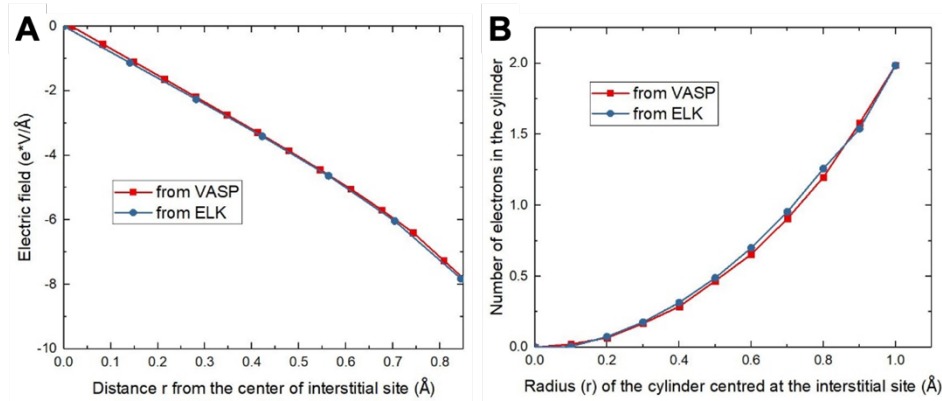


**Fig. S8. Comparison between the results obtained by using pseudopotential-based DFT (VASP) and all-electron code (ELK).** (A) Electric field as a function of the distance from the interstitial center. (B) Number of electrons in the cylinder center at an interstitial site as a function of the radius. The DFT calculations in the main-text, including the calculated charge density in **Fig. 3A**, are obtained using pseudopotentials, which treat the nuclei and core electrons together as screened nuclei with finite radii. To check the accuracy of the pseudopotential-based DFT calculations, we performed all-electron DFT calculations using ELK. The k-mesh is chosen as  $12 \times 12 \times 12$ . The relaxed lattice constant is consistent with that obtained from the pseudopotential-based DFT calculations as shown in **Table S1**. The electron density and electric field is extracted by using an  $80 \times 80 \times 80$  mesh for the unit cell. This comparison results that both the electric field and the numbers of electrons in the interstitial site calculated from the two methods, i.e. VASP and ELK, agree with each other excellently.

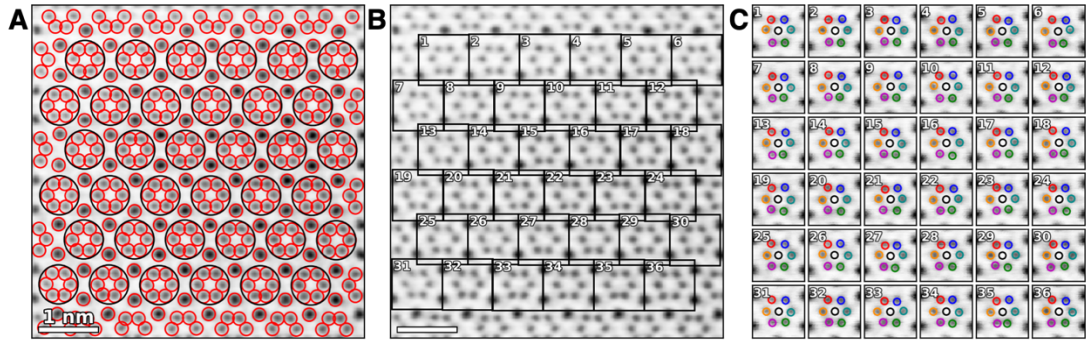


**Fig. S9. Identification of Individual Interstitial Columns.** (A) We create a bright field (BF) image of the electride by integrating the total intensity inside the bright field disk used for the CoM measurements. On this image we use the Python sci-kit learn function `peak_local_max` to identify the positions of all the Y atoms which are clearly observed here. From the list of atoms all neighboring atoms within  $6 \text{ \AA}$  (approximate width of the Y-ring) are determined for each Y atom, and if the same 6 atoms all include each other as neighbors those 6 atoms are determined to be a Y-ring. (B) The position of the 6 ring atoms is then averaged to find the column center with sub-pixel accuracy (even though `peak_local_max` only has pixel-accuracy). From here we use the column centers to interpolate the dataset onto a series of 36  $10 \text{ \AA} \times 10 \text{ \AA}$  areas each with the interstitial column center at the very center of the interpolated region. (C) The result is a series of 36 separate images for the 36 interstitial sites identified in part (A) where the 6 Y-ring atoms and the interstitial column centers fall on the same set of pixel coordinates. Since the dataset is directly based off of the 4D dataset used for the CoM masses we can also use the same coordinates to create individual maps of the field and charge density. As a result, we can directly compare individual sites quantitatively as well as average multiple sites together to improve signal-to-noise.

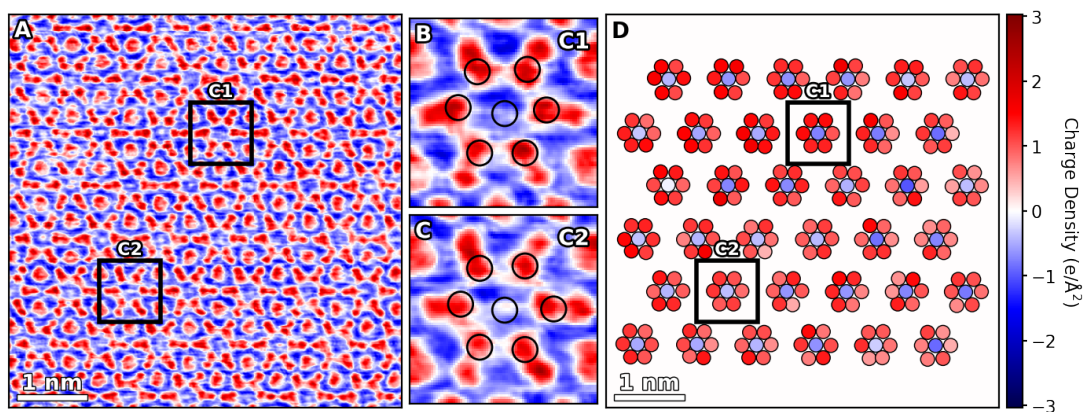


**Fig. S10. Comparison of Column and  $Y_R$  site Charge Density.** While significant variations are clearly observed in the interstitial columns, some variations are also observed in the Y and Si columns surrounding the columns. Here, we determine that the presence of inhomogeneity in anionic columns does not have a direct association with the variation in the surrounding Y atoms. (A) DPC charge density map for the full ROI from which the 36 unit cells are acquired (same as shown in **Fig. 3A** in the main text). Two interstitial columns are highlighted. (B, C) Zoom-in images for the two regions showing difference in intensity inside the column. (D) Measured inhomogeneity of charge density for Y-ring (outer circles) and interstitial column (inner circle). There does not appear to be any notable correlation between columns that have a more neutral column density (i.e. exhibits the inhomogeneity) and the intensity of the surround Y atoms. The column and Y-atom intensities are determined by averaging the measured charge density within a 1 Å radius region around the atomic-positions and column position determined in **Fig. S4**.

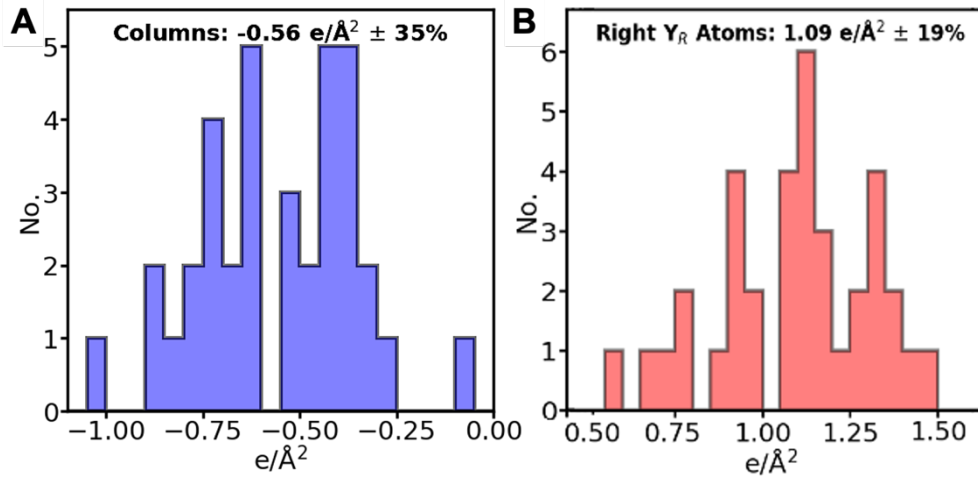


**Fig. S11. Variation of charge density at interstitial columns compared to that of one neighboring  $Y_R$  atomic column.** (A) Histogram of column charge densities (same as shown in Fig. 4a in the main text). (B) The histogram of one neighboring Y atomic column in the Y-rings at each interstitial site. Here, we see that the variation among the interstitial columns is larger than that of the  $Y_R$  sites, with variation coefficient of 35% compared to 19% for  $Y_R$ . Additionally, we believe the other evidences in **Fig. 4** in the main text and **figs. S9, S12, and S13** help corroborating the fact that the inhomogeneity observed is primarily genuine in the material.

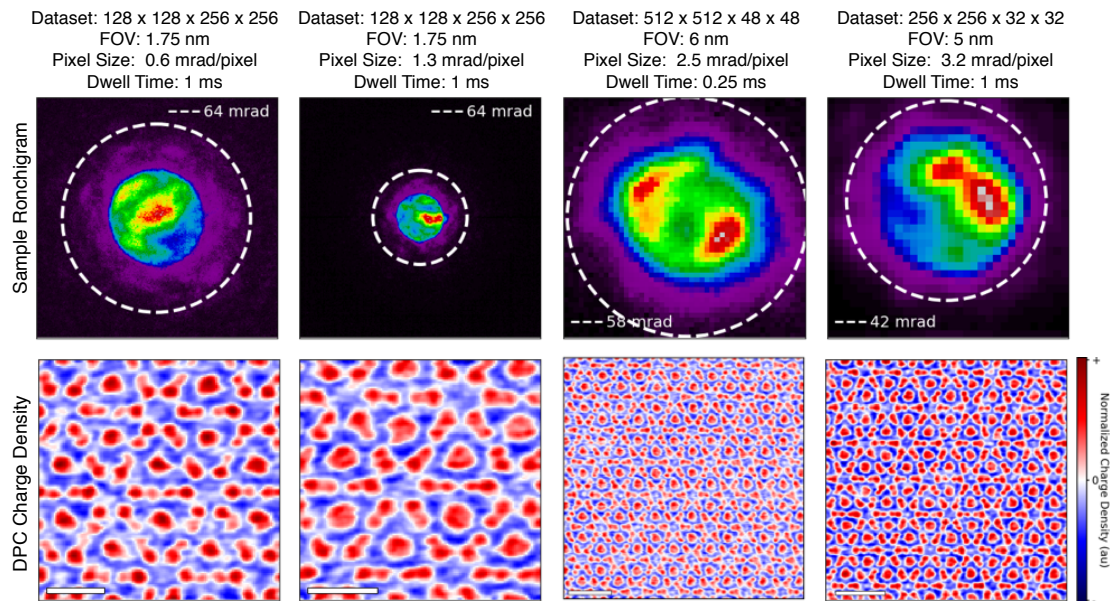


**Fig. S12. DPC charge density maps at different locations and different imaging parameters to validate observed inhomogeneity.** Here we show four different DPC experiments, each in a different location on the sample, and each with a different set of acquisition parameters. The charge inhomogeneity presents itself in random columns regardless of acquisition parameters, pixel size in real-space and momentum-space, and dwell time and across the entire sample.

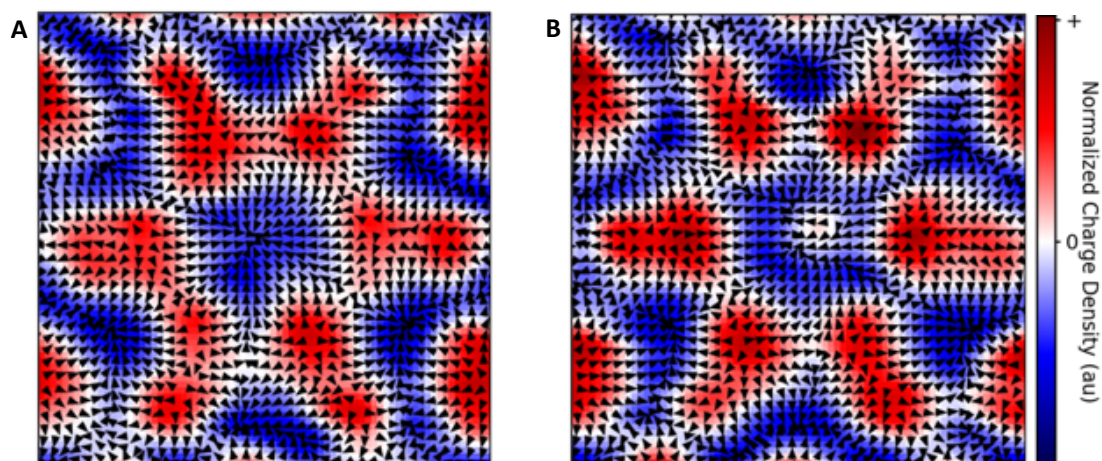


**Fig. S13. Overlaid field and charge density maps to support the observed charge inhomogeneity at anionic sites.** Here we show high magnification images of two different interstitial columns, (A) one with a uniform charge density throughout the column, and (B) one with a significant inhomogeneity. By examining the field in conjunction with the charge density, it can be seen that the inhomogeneity robustly represents itself in the same location in both the fast scan and slow scan direction. In both cases, all field-vectors converge to the very center of the column. As a result, the gradient is radially inward across the entire column and the divergence (and hence the charge density) is constant throughout. In the inhomogeneous case, it can be seen that there is no single convergence point for the field arrows. The arrows converge in an arc around a small circular region in the center of the anionic column. Furthermore, for the field vectors within this circular region divergence can be observed. This arc of convergence tracks around the circular region and depicts the same region to display the convergence in both the fast scan ( $x$ -direction) and the slow-scan ( $y$ -direction). This means that the scanning electron probe that finds and measures the inhomogeneity, is rastered away to probe other parts of the sample, then upon returning to the same column finds the same inhomogeneity of the same magnitude in the same place. The fact that the inhomogeneity is robust to the scan directions, further validates that the inhomogeneity is genuine and not an experimental error. Furthermore, it can be seen that in all other regions surrounding the hexagonal Y-ring, the convergence and divergence points for the fields are the same for both locations, and the inhomogeneity in the column is the only significant difference between the charge density profiles.

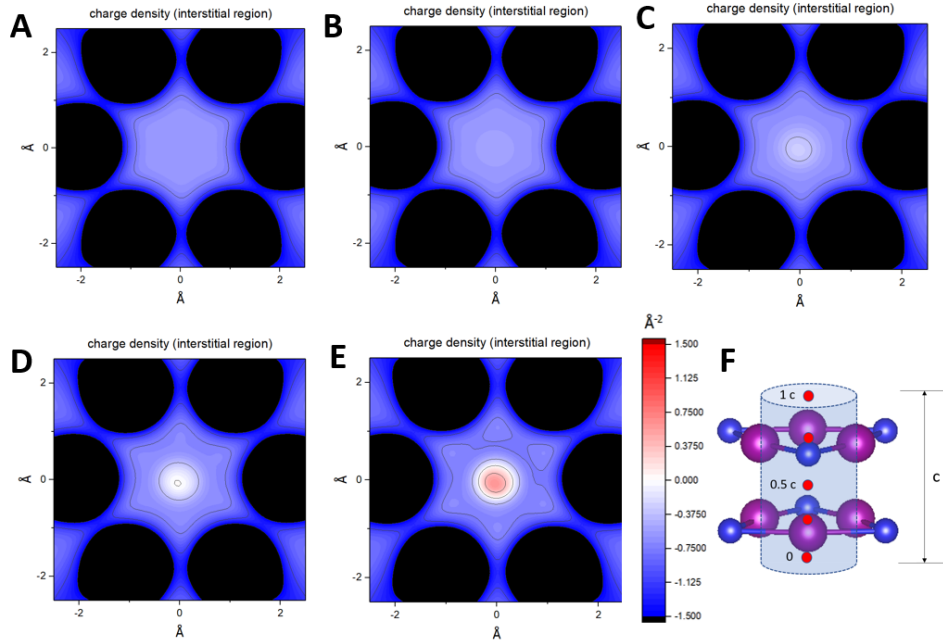


**Fig. S14. DFT calculated charge density with H contamination.** (A-E) represent that 0, 1, 5, 10, and 20 H atoms are contained per 10 unit cells, respectively. Since it is not clear where the H atoms prefer to sit in the interstitial column, three plausible locations along the central axis of the interstitial cylinder were considered, as shown in Figure (F), at the height of 0, 0.25  $c$ , and 0.5  $c$  in a unit cell ( $Y_{10}Si_6$ ), where  $c = 6.38 \text{ \AA}$  is the vertical lattice constant. After relaxation of the three cases (separately conducted using three different unit cells), H atoms in all three cases remain near their initial positions, but the one at around 0.25  $c$  (as well as 0.75  $c$ ) has the lowest energy. Therefore, this position is chosen for further DFT calculations. Methods used to obtain Figs. (B-E) are as follows. Starting from (E), i.e., 20 H atoms per 10 layers (or 2 H per column per unit cell), we put 2 H atoms at the height of 0.25  $c$  and 0.75  $c$  in a unit cell, respectively, and then relax the structure. Two H atoms per unit cell are allowed by the formula  $Y_5Si_3H$  based on a previous literature(2). After that, we plot the charge density in (E). (D) is generated by using 1 H at the location of 0.25  $c$  in a unit cell. (C) is generated by using 1 H in a  $1 \times 1 \times 2$  supercell. To generate (B) and avoid large computational cost, the natural way is by using a  $1 \times 1 \times 10$  supercell that contains 1 H atom. However, since the  $1 \times 1 \times 10$  is very long in the  $c$  dimension, it could spoil convergence since charge sloshing may occur along the long lattice vector. Instead, we regard the charge density of a  $1 \times 1 \times 10$  supercell that contains 1 H atom as the superposition of eight bulk  $1 \times 1 \times 1$  unit cells and one additional  $1 \times 1 \times 2$  supercell containing 1 H atom. In the charge density calculation and lattice relaxation, the electronic k-space integration was performed with the tetrahedron method, involving a  $\Gamma$ -centered  $12 \times 12 \times 16$  k-mesh. For the  $1 \times 1 \times 2$  supercells, the k-mesh is  $12 \times 12 \times 8$ . The unit cell and supercells with H was relaxed with a convergence of  $10^{-8}$  eV for the total energy, and  $10^{-3}$  eV/ $\text{\AA}$  for the forces on each atom. The plane-wave energy cutoff is 500 eV. During relaxation, the lattice parameters are allowed to relax, and the change after relaxation is negligible. Spin magnetization is not considered here as it likely does not affect the charge density in this material.

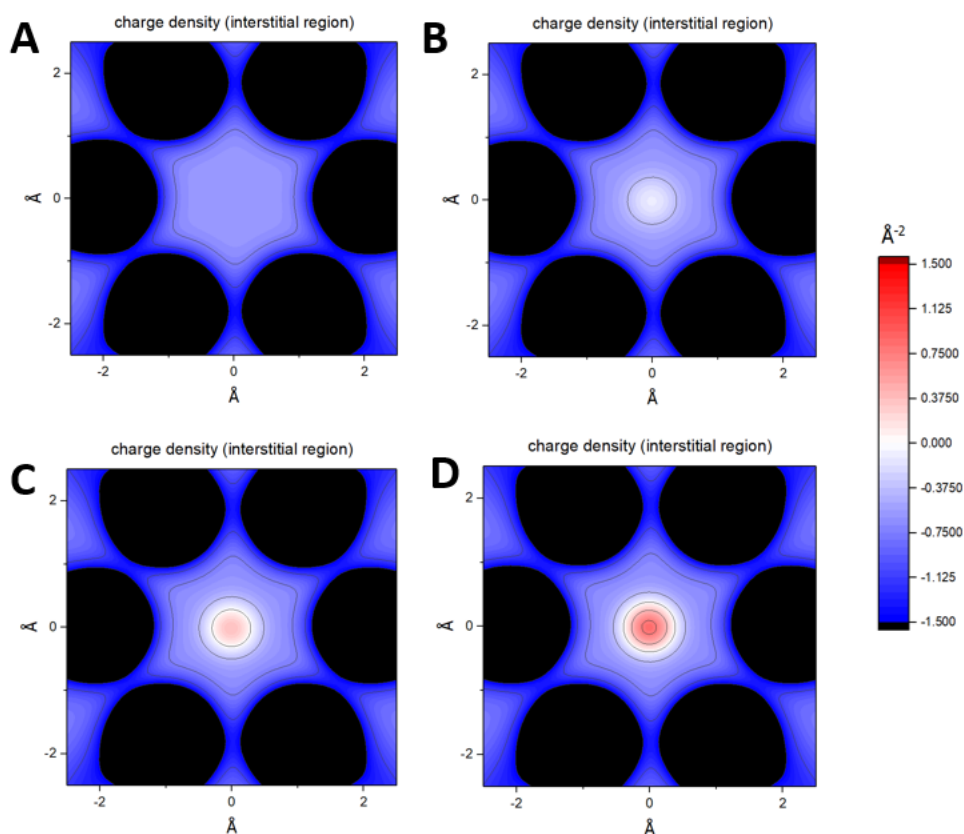


**Fig. S15. DFT calculated charge density with C contamination.** (A-D) represent that 0, 1, 2, and 3 C atoms are contained per 10 interstitial layers, respectively. The method of obtaining these images is similar to that for H-doped  $Y_5Si_3$ . Specifically, (B) is the summation of the charge densities of 5 pure unit cells and one  $1 \times 1 \times 5$  supercell that contains 1 C atom. (C) is charge density of a  $1 \times 1 \times 5$  supercell that contains 1 C atom. (D) is summation of charge density of one pure unit cell and three  $1 \times 1 \times 3$  supercells that contains 1 C atom each. The k-meshes for  $1 \times 1 \times 3$  and  $1 \times 1 \times 5$  supercells are  $12 \times 12 \times 5$  and  $12 \times 12 \times 3$ , respectively. The high contrast a carbon atom contributes is not consistent with the variations of charge intensity at the anionic channels. Thus, the possibility of carbon contamination can be excluded.

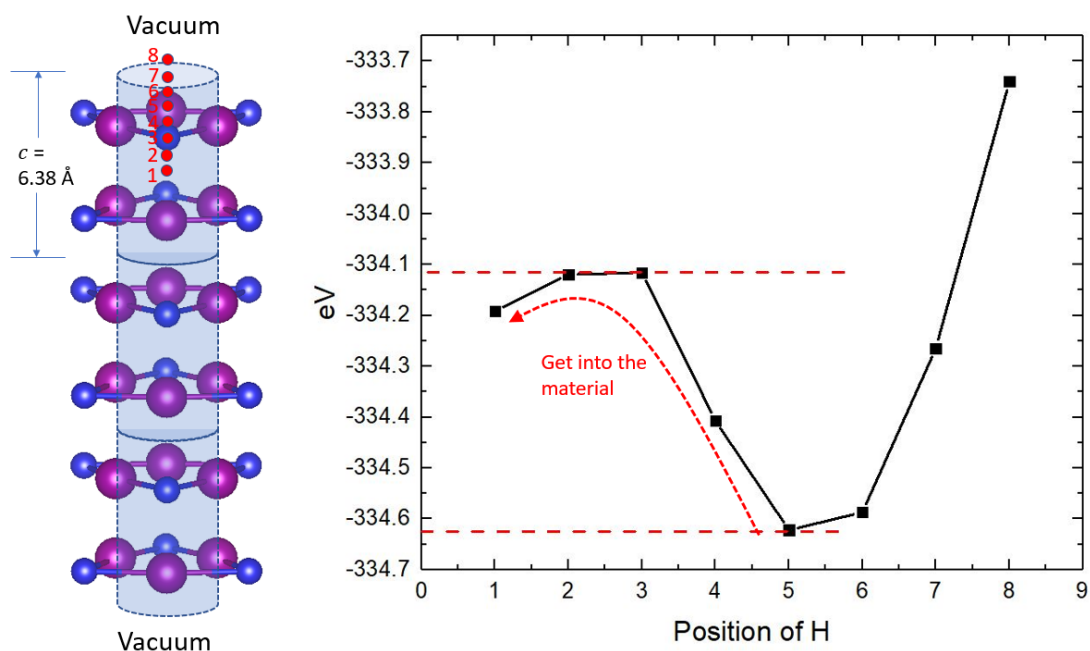


**Fig. S16. DFT calculated energy barrier for H atom to get into the electride  $Y_5Si_3$ .** Firstly, we constructed a  $1 \times 1 \times 3$  supercell and leave the upper and lower plane exposed in vacuum, so that it forms a  $Y_5Si_3$  slab. The vacuum space used in VASP simulation is  $12 \text{ \AA}$ . Then, we relax the slab in VASP until the force of each atom reach below  $0.001 \text{ eV/\AA}$ . After that, we put an H atom at the positions labeled as 1, 2, 3, ..., 8 separately. We fix the z coordinate of the H atoms in the 8 different slabs and relax these slabs. The energies of these slabs after relaxation are plotted in the figure on the right. We can find that, around the Position 5, the system has the lowest energy. To get the H atom into the material (to deeper layers), the H atom need to overcome a barrier of around  $0.5 \text{ eV}$ . Since the pathway we studied is not necessarily the optimal pathway for H migration, the optimal pathway may have even lower energy barrier. Therefore, we conclude that the energy barrier is less than  $0.5 \text{ eV}$ .

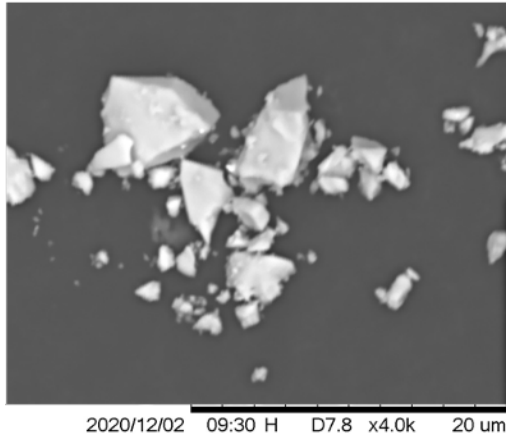


**Fig. S17** SEM image of  $Y_5Si_3$  powder used for experiments shows the majority of the particles have a size of 1-5  $\mu\text{m}$ .

**Table S1. The lattice constant from experiment and DFT calculations.**

<b>Lattice constant</b>	<b><i>a</i> (Å)</b>	<b><i>c</i> (Å)</b>
Experiment (ref 56)	8.410	6.344
Experiment (ref 58)	8.403	6.303
Experiment (ref 59)	8.42	6.32
VASP (PAW-PBE)	8.447	6.380
VASP (PAW-LDA)	8.307	6.225
ELK	8.447	6.380

## REFERENCES AND NOTES

1. S. B. Dawes, D. L. Ward, R. H. Huang, J. L. Dye, First electrider crystal structure. *J. Am. Chem. Soc.* **108**, 3534–3535 (1986).
2. R. H. Huang, M. K. Faber, K. J. Moeggenborg, D. L. Ward, J. L. Dye, Structure of  $K^+$ (cryptand[2.2.2J]) electrider and evidence for trapped electron pairs. *Nature* **331**, 599–601 (1988).
3. J. L. Dye, Electrides: Ionic salts with electrons as the anions. *Science* **247**, 663–668 (1990).
4. D. J. Singh, H. Krakauer, C. Haas, W. E. Pickett, Theoretical determination that electrons act as anions in the electrider  $Cs^+(15\text{-crown-}5)_2 \cdot e^-$ . *Nature* **365**, 39–42 (1993).
5. M. J. Wagner, R. H. Huang, J. L. Eglin, J. L. Dye, An electrider with a large six-electron ring. *Nature* **368**, 726–729 (1994).
6. S. Matsuishi, Y. Toda, M. Miyakawa, K. Hayashi, T. Kamiya, M. Hirano, I. Tanaka, H. Hosono, High-density electron anions in a nanoporous single crystal:  $[Ca_{24}Al_{28}O_{64}]^{4+} \cdot 4e^-$ . *Science* **301**, 626–629 (2003).
7. K. Lee, S. W. Kim, Y. Toda, S. Matsuishi, H. Hosono, Dicalcium nitride as a two-dimensional electrider with an anionic electron layer. *Nature* **494**, 336–340 (2013).
8. J. Park, K. Lee, S. Y. Lee, C. N. Nandadasa, S. Kim, K. H. Lee, Y. H. Lee, H. Hosono, S.-G. Kim, S. W. Kim, Strong localization of anionic electrons at interlayer for electrical and magnetic anisotropy in two-dimensional  $Y_2C$  electrider. *J. Am. Chem. Soc.* **139**, 615–618 (2017).
9. Y. Lu, J. Li, T. Tada, Y. Toda, S. Ueda, T. Yokoyama, M. Kitano, H. Hosono, Water durable electrider  $Y_5Si_3$ : Electronic structure and catalytic activity for ammonia synthesis. *J. Am. Chem. Soc.* **138**, 3970–3973 (2016).
10. Y. Zhang, Z. Xiao, T. Kamiya, H. Hosono, Electron confinement in channel spaces for one-dimensional electrider. *J. Phys. Chem. Lett.* **6**, 4966–4971 (2015).
11. Y. Zhang, H. Wang, Y. Wang, L. Zhang, Y. Ma, Computer-assisted inverse design of inorganic electrides. *Phys. Rev. X* **7**, 011017 (2017).
12. C. Park, S. W. Kim, M. Yoon, First-principles prediction of new electrides with nontrivial band topology based on one-dimensional building blocks. *Phys. Rev. Lett.* **120**, 026401 (2018).
13. M. Hirayama, S. Matsuishi, H. Hosono, S. Murakami, Electrides as a new platform of topological materials. *Phys. Rev. X* **8**, 031067 (2018).
14. M. Kitano, Y. Inoue, Y. Yamazaki, F. Hayashi, S. Kanbara, S. Matsuishi, T. Yokoyama, S.-W. Kim, M. Hara, H. Hosono, Ammonia synthesis using a stable electrider as an electron donor and reversible hydrogen store. *Nat. Chem.* **4**, 934–940 (2012).

15. M. Kitano, S. Kanbara, Y. Inoue, N. Kuganathan, P. V. Sushko, T. Yokoyama, M. Hara, H. Hosono, Electride support boosts nitrogen dissociation over ruthenium catalyst and shifts the bottleneck in ammonia synthesis. *Nat. Commun.* **6**, 6731 (2015).
16. M. Miyakawa, S. W. Kim, M. Hirano, Y. Kohama, H. Kawaji, T. Atake, H. Ikegami, K. Kono, H. Hosono, Superconductivity in an inorganic electride  $12\text{CaO}\cdot 7\text{Al}_2\text{O}_3\cdot e^-$ . *J. Am. Chem. Soc.* **129**, 7270–7271 (2007).
17. Y. Zhang, B. Wang, Z. Xiao, Y. Lu, T. Kamiya, Y. Uwatoko, H. Kageyama, H. Hosono, Electride and superconductivity behaviors in  $\text{Mn}_5\text{Si}_3$ -type intermetallics. *npj Quantum Mater.* **2**, 45 (2017).
18. Y. Lu, J. Wang, J. Li, J. Wu, S. Kanno, T. Tada, H. Hosono, Realization of Mott-insulating electrides in dimorphic  $\text{Yb}_5\text{Sb}_3$ . *Phys. Rev. B* **98**, 125128 (2018).
19. S. W. Kim, T. Shimoyama, H. Hosono, Solvated electrons in high-temperature melts and glasses of the room-temperature stable electride  $[\text{Ca}_{24}\text{Al}_{28}\text{O}_{64}]^{4+}\cdot 4e^-$ . *Science* **333**, 71–74 (2011).
20. I. J. McColm, V. Kotrocv, T. W. Button, N. J. Clark, B. Bruer, Hydrogen sorption properties of  $\text{D}_{8g}$ -type systems: I. Hydrides of  $\text{Y}_5\text{Si}_3$ . *J. Less Common Met.* **115**, 113–125 (1986).
21. I. J. McColm, J. M. Ward, Hydrogen sorption properties of  $\text{D}_{8g}$ -type systems: IV.  $\text{Y}_5\text{Ge}_3$  and  $\text{Y}_5\text{Si}_3$ - $\text{Y}_5\text{Ge}_3$  solid solutions. *J. Alloys Compd.* **178**, 91–100 (1992).
22. X. Zhang, Z. Xiao, H. Lei, Y. Toda, S. Matsuishi, T. Kamiya, S. Ueda, H. Hosono, Two-dimensional transition-metal electride  $\text{Y}_2\text{C}$ . *Chem. Mater.* **26**, 6638–6643 (2014).
23. T. Inoshita, S. Jeong, N. Hamada, H. Hosono, Exploration for two-dimensional electrides via database screening and Ab Initio Calculation. *Phys. Rev. X* **4**, 031023 (2014).
24. Y. Jing, Y. Ma, Y. Li, T. Heine,  $\text{GeP}_3$ : A small indirect band Gap 2D crystal with high carrier mobility and strong interlayer quantum confinement. *Nano Lett.* **17**, 1833–1838 (2017).
25. T. Rojac, A. Bencan, G. Drazic, N. Sakamoto, H. Ursic, B. Jancar, G. Tavcar, M. Makarovic, J. Walker, B. Malic, D. Damjanovic, Domain-wall conduction in ferroelectric  $\text{BiFeO}_3$  controlled by accumulation of charged defects. *Nat. Mater.* **16**, 322–327 (2017).
26. Y. Han, M.-Y. Li, G.-S. Jung, M. A. Marsalis, Z. Qin, M. J. Buehler, L.-J. Li, D. A. Muller, Subnanometre channels embedded in two-dimensional materials. *Nat. Mater.* **17**, 129–133 (2017).
27. O. L. Krivanek, M. F. Chisholm, V. Nicolosi, T. J. Pennycook, G. J. Corbin, N. Dellby, M. F. Murfitt, C. S. Own, Z. S. Szilagy, M. P. Oxley, S. T. Pantelides, S. J. Pennycook, Atom-by-atom structural and chemical analysis by annular dark-field electron microscopy. *Nature* **464**, 571–574 (2010).

28. K. Song, S. Ryu, H. Lee, T. R. Paudel, C. T. Koch, B. Park, J. K. Lee, S.-Y. Choi, Y.-M. Kim, J. C. Kim, H. Y. Jeong, M. S. Rzchowski, E. Y. Tsymbal, C.-B. Eom, S. H. Oh, Direct imaging of the electron liquid at oxide interfaces. *Nat. Nanotechnol.* **13**, 198–203 (2018).
29. H. Lee, N. Campbell, J. Lee, T. J. Asel, T. R. Paudel, H. Zhou, J. W. Lee, B. Noesges, J. Seo, B. Park, L. J. Brillson, S. H. Oh, E. Y. Tsymbal, M. S. Rzchowski, C. B. Eom, Direct observation of a two-dimensional hole gas at oxide interfaces. *Nat. Mater.* **17**, 231–236 (2018).
30. N. Shibata, S. D. Findlay, Y. Kohno, H. Sawada, Y. Kondo, Y. Ikuhara, Differential phase-contrast microscopy at atomic resolution. *Nat. Phys.* **8**, 611–615 (2012).
31. N. Shibata, T. Seki, G. Sánchez-Santolino, S. D. Findlay, Y. Kohno, T. Matsumoto, R. Ishikawa, Y. Ikuhara, Electric field imaging of single atoms. *Nat. Commun.* **8**, 15631 (2017).
32. R. Ishikawa, S. D. Findlay, T. Seki, G. Sánchez-Santolino, Y. Kohno, Y. Ikuhara, N. Shibata, Direct electric field imaging of graphene defects. *Nat. Commun.* **9**, 3878 (2018).
33. J. A. Hachtel, J. C. Idrobo, M. Chi, Sub-Ångstrom electric field measurements on a universal detector in a scanning transmission electron microscope. *Adv. Struct. Chem. Imaging* **4**, 10 (2018).
34. S. Fang, Y. Wen, C. S. Allen, C. Ophus, G. G. D. Han, A. I. Kirkland, E. Kaxiras, J. H. Warner, Atomic electrostatic maps of 1D channels in 2D semiconductors using 4D scanning transmission electron microscopy. *Nat. Commun.* **10**, 1127 (2019).
35. K. Müller, F. F. Krause, A. Béché, M. Schowalter, V. Galioit, S. Löffler, J. Verbeeck, J. Zweck, P. Schattschneider, A. Rosenauer, Atomic electric fields revealed by a quantum mechanical approach to electron picodiffraction. *Nat. Commun.* **5**, 5653 (2014).
36. W. P. Gao, C. Addiego, H. Wang, X. Yan, Y. Hou, D. Ji, C. Heikes, Y. Zhang, L. Li, H. Huyan, T. Blum, T. Aoki, Y. Nie, D. G. Schlom, R. Wu, X. Pan, Real-space charge-density imaging with sub-ångström resolution by four-dimensional electron microscopy. *Nature* **575**, 480–484 (2019).
37. B. Lv, X. Y. Zhu, B. Lorenz, F. Y. Wei, Y. Y. Xue, Z. P. Yin, G. Kotliar, C. W. Chu, Superconductivity in the  $Mn_5Si_3$ -type  $Zr_5Sb_3$  system. *Phys. Rev. B* **88**, 134520 (2013).
38. K. Müller-Caspary, F. F. Krause, T. Grieb, S. Löffler, M. Schowalter, A. Béché, V. Galioit, D. Marquardt, J. Zweck, P. Schattschneider, J. Verbeeck, A. Rosenauer, Measurement of atomic electric fields and charge densities from average momentum transfers using scanning transmission electron microscopy. *Ultramicroscopy* **178**, 62–80 (2017).
39. G. Sánchez-Santolino, N. R. Lugg, T. Seki, R. Ishikawa, S. D. Findlay, Y. Kohno, Y. Kanitani, S. Tanaka, S. Tomiya, Y. Ikuhara, N. Shibata, Probing the internal atomic charge density distributions in real space. *ACS Nano* **12**, 8875–8881 (2018).

40. P. Ehrenfest, Bemerkung über die angenäherte Gültigkeit der klassischen Mechanik innerhalb der Quantenmechanik. *Z. Phys.* **45**, 455–457 (1927).
41. A. Lubk, J. Zweck, Differential phase contrast: An integral perspective. *Phys. Rev. A* **91**, 023805 (2015).
42. M. C. Cao, Y. M. Han, Z. Chen, Y. Jiang, K. X. Nguyen, E. Turgut, G. D. Fuchs, D. A. Muller, Theory and practice of electron diffraction from single atoms and extended objects using an EMPAD. *Microscopy* **67**, i150–i161 (2018).
43. A. Togo, I. Tanaka, First principles phonon calculations in materials science. *Scripta Mater.* **108**, 1–5 (2015).
44. Y. Q. Cheng, L. L. Daemen, A. I. Kolesnikov, A. J. Ramirez-Cuesta, Simulation of inelastic neutron scattering spectra using OCLIMAX. *J. Chem. Theory Comput.* **15**, 1974–1982 (2019).
45. Z. D. Hood, Y. Q. Cheng, S. F. Evans, S. P. Adhikari, M. P. Paranthaman, Unraveling the structural properties and dynamics of sulfonated solid acid carbon catalysts with neutron vibrational spectroscopy. *Catal. Today* **358**, 387–393 (2020).
46. E. C. Regan, D. Wang, C. Jin, M. I. B. Utama, B. Gao, X. Wei, S. Zhao, W. Zhao, Z. Zhang, K. Yumigeta, M. Blei, J. D. Carlström, K. Watanabe, T. Taniguchi, S. Tongay, M. Crommie, A. Zettl, F. Wang, Mott and generalized Wigner crystal states in  $WSe_2/WS_2$  moiré superlattices. *Nature* **579**, 359–363 (2020).
47. Y. H. Jiang, X. Y. Lai, K. Watanabe, T. Taniguchi, K. Haule, J. H. Mao, E. Y. Andrei, Charge order and broken rotational symmetry in magic-angle twisted bilayer graphene. *Nature* **573**, 91–95 (2019).
48. A. Ohtomo, H. Y. Hwang, A high-mobility electron gas at the  $LaAlO_3/SrTiO_3$  heterointerface. *Nature* **427**, 423–426 (2004).
49. S. Gariglio, N. Reyren, A. D. Caviglia, J.-M. Triscone, Superconductivity at the  $LaAlO_3/SrTiO_3$  interface. *J. Phys. Condens. Matter* **21**, 164213 (2009).
50. L. Akselrud, Y. Grin, WinCSD: Software package for crystallographic calculations (Version 4). *J. Appl. Cryst.* **47**, 803–805 (2014).
51. G. Kresse, J. Hafner, Ab initio molecular dynamics for liquid metals. *Phys. Rev. B* **47**, 558–561 (1993).
52. The Elk Code; <http://elk.sourceforge.net/>.
53. P. E. Blöchl, Projector augmented-wave method. *Phys. Rev. B* **50**, 17953–17979 (1994).
54. J. P. Perdew, K. Burke, M. Ernzerhof, Generalized gradient approximation made simple. *Phys. Rev. Lett.* **77**, 3865–3868 (1996).

55. L. J. Allen, A. J. D'Alfonso, S. D. Findlay, Modelling the inelastic scattering of fast electrons. *Ultramicroscopy* **151**, 11–22 (2015).
56. E. Parthé, The crystal structure of  $Y_5Si_3$  and  $Y_5Ge_3$ . *Acta Crystallogr.* **13**, 868–871 (1960).
57. H.-R. Zhang, R. F. Egerton, M. Malac, Local thickness measurement through scattering contrast and electron energy-loss spectroscopy. *Micron* **43**, 8–15 (2012).
58. J. Roger, M. Ben Yahia, V. Babizhetskyy, J. Bauer, S. Cordier, R. Guérin, K. Hiebl, X. Rocquefelte, J. Y. Saillard, J. F. Halet,  $Mn_5Si_3$ -type host-interstitial boron rare-earth metal silicide compounds  $RE_5Si_3$ : Crystal structures, physical properties and theoretical considerations. *J. Solid State Chem.* **179**, 2310–2328 (2006).
59. I. Mayer, I. Shidlovsky,  $M_5X_3$ -type rare earth silicides and germanides and their ternary phases with carbon. *Inorg. Chem.* **8**, 1240–1243 (1969).